The Astrophysical Journal Supplement Series, 155:33–72, 2004 November

THE VSOP 5 GHz ACTIVE GALACTIC NUCLEUS SURVEY. III. IMAGING RESULTS FOR THE FIRST 102 SOURCES

W. K. Scott,[1] E. B. Fomalont,[2] S. Horiuchi,[3,4,5] J. E. J. Lovell,[6] G. A. Moellenbrock,[7]
R. G. Dodson,[8,9] P. G. Edwards,[9] G. V. Coldwell,[10] S. Fodor,[3,11] S. Frey,[12] L. I. Gurvits,[13]
H. Hirabayashi,[9] M. L. Lister,[2] L. Mosoni,[12,14] Y. Murata,[9] Z. Paragi,[12,13]
B. G. Piner,[11] Z.-Q. Shen,[9,15,16] A. R. Taylor,[1] and S. J. Tingay[5,6]
Received 2004 January 19; accepted 2004 May 7

ABSTRACT

The VLBI Space Observatory Programme (VSOP) mission is a Japanese-led project to study radio sources with sub-milliarcsec resolution using an orbiting 8 m telescope, *HALCA*, along with global arrays of Earth-based telescopes. Approximately 25% of the observing time is devoted to a survey of compact active galactic nuclei (AGNs) that are stronger than 1 Jy at 5 GHz—the VSOP AGN Survey. This paper, the third in the series, presents the results from the analysis of the first 102 Survey sources. We present high-resolution images and plots of visibility amplitude versus projected baseline length. In addition, model-fit parameters to the primary radio components are listed, and from these the angular size and brightness temperature for the radio cores are calculated. For those sources for which we were able to determine the source frame core brightness temperature, a significant fraction (53 out of 98) have a source frame core brightness temperature in excess of 10^{12} K. The maximum source frame core brightness temperature we observed was 1.2×10^{13} K. Explaining a brightness temperature this high requires an extreme amount of relativistic Doppler beaming. Since the maximum brightness temperature one is able to determine using only ground-based arrays is of the order of 10^{12} K, our results confirm the necessity of using space VLBI to explore the extremely high brightness temperature regime.

Subject headings: galaxies: active — radio continuum: galaxies — surveys

Online material: color figure, machine-readable tables

1. INTRODUCTION

On 1997 February 12, the Institute of Space and Astronautical Science launched the *HALCA* (*Highly Advanced Laboratory for Communications and Astronomy*) satellite, which contained an 8 m telescope, dedicated specifically to VLBI. With an apogee height of 21,400 km, radio sources are imaged with angular resolution 3 times greater than with ground arrays at the same frequency (Hirabayashi et al. 1998). About 25% of the observing time was dedicated to the VSOP (VLBI Space Observatory Programme) Survey of approximately 400 flat-spectrum active galactic nuclei (AGNs) that are stronger than 1 Jy at 5 GHz. Those 294 sources which had compact structures suitable for observations with VSOP were designated the VSOP Source Sample (VSS; Fomalont et al. 2000b; Edwards et al. 2002). The compilation and general description of the VSOP AGN Survey is given by Hirabayashi et al. (2000b, hereafter Paper I) and Fomalont et al. (2000b). The major goal of the Survey is to determine statistical properties of the sub-milliarcsecond structure of the strongest extragalactic radio sources at 5 GHz and to compare these structures with other properties of the sources. Combined with ground observations at many radio frequencies (single-dish and VLBI), and at higher energies, the Survey will provide an invaluable list for further detailed ground-based studies, as well as a list of sources to be observed in future space VLBI missions.

This paper is the third of the VSOP Survey series. Lovell et al. (2004, hereafter Paper II) describes the reduction of the data and the specific problems associated with reducing space VLBI data. In this paper, we present the results of 102 sources in the VSS list for which the data reduction is now complete. The results include an image and a simple model for each

[1] Physics and Astronomy Department, University of Calgary, 2500 University Drive NW, Calgary, AL T2N 1N4, Canada; bill@ras.ucalgary.ca, russ@ras.ucalgary.ca.
[2] National Radio Astronomy Observatory, 520 Edgemont Road, Charlottesville, VA 22903; efomalon@nrao.edu, mlister@nrao.edu.
[3] Jet Propulsion Laboratory, 4800 Oak Grove Drive, Pasadena, CA 91109.
[4] National Astronomical Observatory of Japan, 2-21-1 Osawa, Mitaka, Tokyo 181-8588, Japan.
[5] Centre for Astrophysics and Supercomputing, Swinburne University of Technology, P.O. Box 218, Hawthorn, VIC 3122, Australia; stingay@astro.swin.edu.au, shoriuchi@astro.swin.edu.au.
[6] Australia Telescope National Facility, Commonwealth Scientific and Industrial Research Organization, P.O. Box 76, Epping, NSW 2122, Australia; jim.lovell@csiro.au.
[7] National Radio Astronomy Observatory, P.O. Box O, Socorro, NM 87801; gmoellen@nrao.edu.
[8] School of Mathematics and Physics, University of Tasmania, GPO Box 252-21, Hobart, TAS 7001, Australia.
[9] Institute of Space and Astronautical Science, Japan Aerospace Exploration Agency, 3-1-1 Yoshinodai, Sagamihara, Kanagawa 229-8510, Japan; rdodson@vsop.isas.jaxa.jp, pge@vsop.isas.jaxa.jp, hirax@vsop.isas.jaxa.jp, murata@vsop.isas.jaxa.jp.
[10] Grupo de Investigaciones en Astronomia Teórica y Experimental, Observatorio Astronómico, Universidad Nacional de Córdoba, Laprida 854, 5000 Córdoba, Argentina; georgina@oac.uncor.edu.
[11] Physics Department, Whittier College, 13406 East Philadelphia, P.O. Box 634, Whittier, CA 90608-4413; gpiner@whittier.edu, fodor_zie@yahoo.com.
[12] FÖMI Satellite Geodetic Observatory, P.O. Box 585, H-1592 Budapest, Hungary; frey@sgo.fomi.hu.
[13] Joint Institute for VLBI in Europe, P.O. Box 2, 7990 AA Dwingeloo, The Netherlands; lgurvits@jive.nl, zparagi@jive.nl.
[14] MTA Konkoly Observatory, P.O. Box 67, H-1525 Budapest, Hungary; mosoni@konkoly.hu.
[15] Shanghai Astronomical Observatory, National Astronomical Observatories, Chinese Academy of Sciences, Shanghai 200030, China; zshen@ center.shao.ac.cn.
[16] Institute of Astronomy and Astrophysics, Academia Sinica, P.O. Box 23-141, Taipei 106, Taiwan.

source, and the observed distribution of radio core sizes and brightness temperatures. Horiuchi et al. (2004, hereafter Paper IV) contains a statistical analysis using the visibility data.

In § 2 we briefly describe the source list compilation, the observations, and data reduction. This information is provided in more detail in other VSOP Survey papers. The presentation of the results is given in graphical and tabular form in § 3. The discussion of the source structures, with emphasis on the radio cores and source brightness temperatures, is given in § 4.

2. SOURCE SAMPLE, OBSERVATIONS, AND DATA REDUCTION

The description of the VSOP mission and the 5 GHz AGN Survey has been given in Hirabayashi et al. (1998, 2000a, 2000b) and Fomalont et al. (2000a) and therefore will only be briefly summarized here. In order to be included in the VSOP Survey a source was required to have the following characteristics:

1. a total flux density at 5 GHz, $S_5 \geq 5.0$ Jy; or
2. a total flux density at 5 GHz, $S_5 \geq 0.95$ Jy; and
3. a spectral index $\alpha \geq -0.45$ ($S \propto \nu^{\alpha}$); and
4. a Galactic latitude $|b| \geq 10^{\circ}$.

The finding surveys from which sources were selected were primarily the Green Bank GB6 Catalog for the northern sky (Gregory et al. 1996), and the Parkes-MIT-NRAO (PMN) Survey (Lawrence et al. 1986; Griffith & Wright 1993) for the southern sky. The 402 sources satisfying these criteria comprise the VSOP source list (Hirabayashi et al. 2000b).

However, it was expected that many sources in the VSOP source list would not be detectable by *HALCA* because of insufficient correlated flux on the longest baselines. Hence, most sources with declination greater than -44° were observed in a VLBA prelaunch survey (VLBApls; Fomalont et al. 2000a). Based upon the VLBApls results a cutoff criterion, a minimum flux density of 0.32 Jy at 140 Mλ, was established for inclusion of a source in the Survey (Fomalont et al. 2000b). Those sources exceeding this threshold, as well as those sources south of -44°, were designated the VSOP Source Sample (VSS) and were scheduled for VSOP observations. The VSS contains 294 sources, 289 in the original sample (Hirabayashi et al. 2000b), plus five extra sources that were added after it was discovered that their VLBA observations suffered from insufficiently accurate positional information (Edwards et al. 2002). These sources do not comprise a rigidly defined complete sample, and the VSS is discussed in more detail in Paper IV, where a statistical analysis of the visibility data is undertaken.

Observations of the VSS began in 1997 August, with the most recent observations being made in 2003 October. However, a subsequent loss of attitude control of the *HALCA* satellite has prevented any further observations as of the time of writing (although it is hoped that attitude control may again be regained, in which case Survey observations will be resumed). In this paper we present the analysis of the 102 experiments successfully reduced by the end of 2002. The observing parameters for these 102 experiments can be found in Table 1. A typical experiment uses two to five ground-based telescopes plus *HALCA*, with a total observation time per source of approximately 4 hr.

In addition, for those sources in the VSS that were also included in scientific general observing time (GOT) proposals, a subset of the data was extracted for use in the Survey. To be comparable with the Survey data were extracted from typically three or four GRTs (ground radio telescopes), and covered about 4 hr of observation time. Approximately 100 sources in the VSS have GOT extracted data. Of the 102 sources described in this paper, 56 have GOT extracted data. The GRTs of choice for most data extraction experiments with the VLBA as the ground-based array were Mauna Kea and St. Croix, the GRTs that provided the longest ground baselines.

A chart indicating the status of all the 289 Survey experiments as of the end of 2002 is given in Figure 1. A somewhat higher percentage of stronger Survey sources are completed because the data for many of these were extracted from GOT proposals, and these had higher priority in scheduling than Survey experiments. Typically, these experiments tended to look at the stronger "famous" radio sources. There was also some attempt to schedule with a higher priority those Survey sources having a total flux density greater than 1.3 Jy. Nevertheless, the date for scheduling any specific experiment was randomized to some extent. First, there were *HALCA* constraints that limited the area of sky that could be observed on any given date. Second, the period when reasonable (u, v) coverage for the target source could be achieved had an 18 month cycle. Thus, the distribution of the 102 sources given in this paper should be reasonably representative of the AGN sample.

All calibration and editing of the data were carried out using the AIPS software package (Greisen 1988), while Difmap (Shepherd 1997) was used to image the data. The calibration, editing, and imaging of the VSOP Survey data are described fully elsewhere (Moellenbrock et al. 2000; Lovell et al. 2004). Since most of the sources, especially those with $\delta > -44^{\circ}$, have been imaged with previous ground VLBI observations, consistency of the VSOP image with these other images was used to constrain the cleaning and modeling. The results of, and supporting documentation for, the data reduction can be found on the VSOP Web site.[17] The calibrated data are available from ISAS on request.

3. THE RESULTS

3.1. *The Visibility Amplitudes and Images*

The graphical results of the data reduction are shown in Figure 2. For each source three separate panels are presented horizontally across the page, the (u, v) coverage, the correlated flux density versus (u, v) radius, and the cleaned image. The quality of the images varies considerably. However, even for sources that have only two GRTs, the major structural details of the core can be ascertained, albeit with some loss of sensitivity to larger scale radio emission.

The fidelity of these images is limited by two factors, the effect of the (u, v) plane undersampling, and the uncertainty in the amplitude calibration.

Because of the length of time necessary for the satellite to slew between sources, *HALCA* was not able to participate in fringe-finder or flux-calibrator scans scheduled in the VSOP observations. Amplitude self-calibration was possible for images made with the data from four or more antennas. However, for the Survey the number of baselines was often insufficient to perform this. The amplitude calibration is therefore often entirely derived from the measured or expected gain and system temperatures of the antennas.

Although the amplitude scale of the VSOP Survey data was calibrated during the data reduction stage (Lovell et al. 2004),

[17] See http://www.vsop.isas.jaxa.jp/survey.

TABLE 1

SURVEY EXPERIMENT DETAILS

SOURCE NAMES						TIME ON SOURCE	*HALCA* TIME ON SOURCE				
J2000 (1)	B1950 (2)	OBS. CODE (3)	OBS. DATE (4)	GRTS (5)	TSS (6)	(hh:mm) (7)	(hh:mm) (8)	CORR. (9)	ID (10)	z (11)	REFERENCES (12)
J0006−0623.....	0003−066	vs03t	1998 Aug 29	THM	R	2:15	2:00	P	B	0.347	123
J0019+7327.....	0016+731	vs07a	1998 Mar 02	lms	GN	4:30	2:30	S	Q	1.781	12357
J0042+2320.....	0039+230	vs07u	1999 Aug 12	MS	N	2:30	2:30	P	E	...	124
J0106−4034.....	0104−408	vs03s	1998 Jun 08	HM	R	3:30	3:30	P	Q	0.584	12
J0115−0127.....	0112−017	vs07t	1999 Aug 10	TMS	GRT	3:45	3:45	P	Q	1.365	1234
J0121+1149.....	0119+115	vs08p	2001 Jul 22	RS	R	2:30	2:30	P	Q	0.570	123
J0126+2559.....	0123+257	vs08o	2001 Jul 20	RS	U	3:15	3:15	P	Q	2.370	12
J0136+4751.....	0133+476	vs03r	1999 Aug 16	mnps	R	4:30	4:30	S	Q	0.859	123457
J0210−5101.....	0208−512	vs03a	1998 Jun 10	ATm	TG	4:15	4:15	P	B	1.003	6
J0217+7349.....	0212+735	vs02o	1997 Sep 05	pmh	N	2:15	2:15	S	Q	2.367	12357
J0251+4315.....	0248+430	vs07q	1999 Feb 15	EJP	NR	0:45	0:45	S	Q	1.310	124
J0319+4130.....	3C 84	vs01c	1998 Aug 25	hkms	GT	4:00	4:00	S	G	0.017	157
J0334−4008.....	0332−403	vs04b	1998 Jul 10	HU	R	3:00	3:00	P	B	1.445*	1
J0348−2749.....	0346−279	vs08m	2001 Aug 09	CMS	U	2:00	1:30	P	Q	0.987	1
J0403−3605.....	0402−362	vs03z	1998 Jul 30	CH	N	1:30	1:30	P	Q	1.417	4
J0405−1308.....	0403−132	vs03e	1998 Aug 19	MS	GR	3:45	3:15	P	Q	0.571	124
J0423−0120.....	0420−014	vs02g	1999 Feb 04	bhp	T	4:00	4:00	S	Q	0.915	123
J0440−4333.....	0438−436	vs01r	1998 Mar 07	AHM	R	3:30	3:30	M	Q	2.852	146
J0453−2807.....	0451−282	vs04g	1999 Sep 12	KM	G	3:30	3:30	M	Q	2.560	1
J0457−2324.....	0454−234	vs05n	2002 Feb 27	KMT	U	3:45	1:00	P	Q	1.003	14
J0501−0159.....	0458−020	vs02z	1999 Sep 22	AKM	R	2:15	2:15	P	Q	2.286	123
J0538−4405.....	0537−441	vs02c	1998 Mar 01	HTM	N	2:30	2:30	M	Q	0.896	26
J0539−2839.....	0537−286	vs10g	1999 Oct 01	AHTM	GU	3:00	2:15	P	Q	3.104	14
J0542+4951.....	3C 147	vs01p	1999 Mar 18	RSPU	NTU	8:00	5:30	M	Q	0.545	12
J0555+3948.....	0552+398	vs01n	1999 Mar 23	bnS	G	2:15	2:15	S	Q	2.363	1234
J0607−0834.....	0605−085	vs03p	1999 Jan 14	HTKMS	RT	7:45	5:00	P	Q	0.872	123
J0609−1542.....	0607−157	vs02a	1998 Apr 04	HTMSU	R	4:30	0:30	P	Q	0.324	123
J0635−7516.....	0637−752	vs01t	1997 Nov 21	AHM	G	5:00	3:45	P	Q	0.651	6
J0714+3534.....	0711+356	vs09k	1999 Apr 09	hmo	NT	5:00	4:00	S	Q	1.620	12457
J0738+1742.....	0735+178	vs05d	1999 Jan 30	bmps	G	2:45	2:30	S	B	0.424	123
J0741+3112.....	0738+313	vs02k	1999 Jan 10	mns	T	2:30	2:30	S	Q*	0.631*	123
J0748+2400.....	0745+241	vs10d	1999 Feb 09	KMS	U	3:00	3:00	M	G	0.409	123
J0811+0146.....	0808+019	vs07n	1999 Jan 07	bmp	T	2:00	2:00	S	B	0.930*	123
J0818+4222.....	0814+425	vs06g	1999 Apr 24	lms	NT	3:00	3:00	S	B	0.245*	12357
J0824+5552.....	0820+560	vs09i	2000 Oct 15	RKN	TU	2:30	2:30	M	Q	1.417	12
J0836−2016.....	0834−201	vs02y	1999 Jan 23	HTKMS	RT	5:15	0:45	P	Q	2.752	13
J0841+7053.....	0836+710	vs04e	1997 Oct 07	lms	RT	5:30	3:45	S	Q	2.218	12357
J0854+2006.....	OJ 287	vs03y	1999 Apr 04	bEfs	G	4:00	4:00	S	B	0.306	123
J0903+4651.....	0859+470	vs09g	1999 Feb 14	EGO	T	5:15	1:00	S	Q	1.462	12357
J0909+0121.....	0906+015	vs11r	1999 Jan 09	TMS	T	4:45	3:00	P	Q	1.018	123
J0920+4441.....	0917+449	vs07x	1999 Feb 07	bfms	T	4:00	3:15	S	Q	2.180	123
J0927+3902.....	4C 39.25	vs01f	1997 Oct 23	msY	R	2:45	1:45	S	Q	0.698	123457
J1037−2934.....	1034−293	vs05t	1999 Jun 02	hos	G	2:45	2:45	S	Q	0.312	124
J1048+7143.....	1044+719	vs04j	1999 Apr 28	SP	GTU	4:15	3:30	M	Q	1.150	12
J1058+0133.....	1055+018	vs02l	1999 May 12	Ehns	N	3:00	3:00	S	Q	0.888	1234
J1107−4449.....	1104−445	vs02v	1999 May 27	ATS	RU	3:15	2:00	P	Q	1.598	6
J1118+1234.....	1116+128	vs05s	1997 Dec 17	KMNSU	NT	4:15	2:00	P	Q	2.118	124
J1146−2447.....	1143−245	vs06w	1999 May 26	HTS	RU	7:45	6:45	M	Q	1.940	12
J1147−0724.....	1145−071	vs09x	2000 Mar 08	TKM	GT	5:30	4:15	P	Q	1.342	123
J1147−3812.....	1144−379	vs04d	1997 Dec 28	TmM	G	3:45	3:45	P	Q	1.048	12
J1215−1731.....	1213−172	vs05a	1998 Jan 11	GHN	RT	3:30	0:45	M	G*	...	124
J1229+0203.....	3C 273B	vs01b	1997 Dec 22	blmns	NR	4:15	4:15	S	Q	0.158	13
J1230+1223.....	3C 274,M87	vs01a	1997 Dec 20	bmps	NR	4:00	3:30	S	G	0.004	123
J1246−2547.....	1244−255	vs04r	1998 Jan 21	HTMSU	GT	2:45	2:45	P	Q	0.638	14
J1256−0547.....	3C 279	vs01g	1998 Jan 10	kms	R	2:00	2:00	S	Q	0.538	123
J1310+3220.....	1308+326	vs02e	1998 Jun 29	hns	T	1:30	1:00	S	Q	0.997	1234
J1337−1257.....	1334−127	vs01y	1999 Jul 10	bfms	T	3:15	2:30	S	Q	0.539	123
J1357−1744.....	1354−174	vs08j	1998 Jan 30	AHMU	GT	4:45	2:30	P	Q	3.147	14
J1407+2827.....	OQ 208	vs03o	1998 Jun 30	Ehs	T	1:15	1:15	S	G	0.077	123
J1430+1043.....	1427+109	vs09c	2001 Jan 18	CHMNS	T	7:15	3:15	P	Q	1.710	1
J1507−1652.....	1504−166	vs03m	1998 Apr 10	HMU	NT	4:30	1:45	P	Q	0.876	123
J1510−0543.....	1508−055	vs06t	1998 Apr 16	TU	GNT	1:45	1:45	P	Q	1.191	134

TABLE 1—*Continued*

Source Names						Time on Source	*HALCA* Time on Source				
J2000 (1)	B1950 (2)	Obs. Code (3)	Obs. Date (4)	GRTs (5)	TSs (6)	(hh:mm) (7)	(hh:mm) (8)	Corr. (9)	ID (10)	z (11)	References (12)
J1512−0905.....	1510−089	vs02x	1999 Aug 11	mos	GT	2:30	2:30	S	Q*	0.360*	1234
J1517−2422.....	1514−241	vs03u	1998 Apr 27	HTU	GNU	7:30	4:30	P	B	0.048	123
J1549+0237.....	1546+027	vs06e	1998 Jul 31	GH	RU	3:00	2:00	P	Q	0.412	1234
J1613+3412.....	1611+343	vs02b	1998 Feb 04	mn	GT	7:00	6:00	M	Q	1.401	123
J1617−7717.....	1610−771	vs02u	1999 Apr 05	AM	T	3:30	3:00	P	Q	1.710	6
J1626−2951.....	1622−297	vs03l	1998 Feb 22	HTS	T	1:15	1:15	P	Q	0.815	146
J1635+3808.....	1633+382	vs03d	1998 Aug 04	bmns	RT	4:30	4:30	S	Q	1.807	12357
J1638+5720.....	1637+574	vs06n	1998 Apr 21	hlm	N	4:00	4:00	S	Q	0.751	1257
J1640+3946.....	NRAO 512	vs08y	1999 Sep 03	KN	R	1:00	1:00	P	Q	1.666	1234
J1642+3948.....	3C 345	vs01k	1998 Jul 28	bmns	RT	3:45	3:15	S	Q	0.594	1235
J1642+6856.....	1642+690	vs07w	1998 May 31	ENS	GT	5:45	4:15	S	G	0.751	12357
J1653+3945.....	Mrk 501	vs08h	1998 Apr 07	hlm	NR	3:15	3:15	S	B	0.033	12357
J1658+0515.....	1656+053	vs05i	1998 Mar 04	HTMS	GT	4:00	8:45	P	Q	0.879	1234
J1658+0741.....	1655+077	vs07g	1998 Mar 05	HTMNS	GNT	7:15	2:30	P	Q	0.621	1234
J1723−6500.....	1718−649	vs02f	1999 Mar 25	AHT	NT	3:00	0:15	P	G	0.014	6
J1733−1304.....	NRAO 530	vs01m	1997 Sep 08	AMU	U	3:30	3:30	P	Q	0.902	123
J1740+5211.....	1739+522	vs10v	1998 Jun 14	mns	NR	3:30	3:30	S	Q	1.379	12357
J1751+0939.....	1749+096	vs04o	1998 Aug 20	hmn	R	2:30	2:30	S	Q	0.320	123
J1800+7828.....	1803+784	vs02w	1997 Oct 16	hlm	R	3:00	3:00	S	Q	0.680	12357
J1806+6949.....	3C 371	vs04x	1998 Mar 11	hmns	NT	4:30	4:30	S	B	0.050	12357
J1824+5651.....	1823+568	vs06d	1998 May 31	EGN	R	4:30	2:30	S	Q	0.663	12357
J1902+3159.....	3C 395	vs06c	1998 May 01	hnps	N	4:30	4:30	S	Q	0.635	123
J1924−2914.....	1921−293	vs01e	1998 Jun 19	los	R	1:45	1:45	S	Q	0.352	1234
J1939−1525.....	1936−155	vs06m	1998 Jul 22	HTS	GT	4:30	3:15	P	Q	1.657	124
J2000−1748.....	1958−179	vs04w	1998 Jun 25	TS	NT	2:30	2:30	P	Q	0.652	124
J2005+7752.....	2007+777	vs06r	1998 Mar 10	bfms	G	3:00	2:00	S	B	0.342	1234
J2022+6136.....	2021+614	vs02q	1997 Nov 06	hkm	T	4:15	4:15	S	G	0.227	123457
J2101+0341.....	2059+034	vs08v	2000 Nov 14	KS	R	1:45	1:45	P	Q	1.015	124
J2129−1538.....	2126−158	vs08e	1998 Jul 13	fmnps	GR	3:00	3:00	S	Q	3.280	124
J2136+0041.....	2134+004	vs01h	1997 Nov 28	TMU	T	3:45	2:15	P	Q	1.932	123
J2158−1501.....	2155−152	vs03g	1998 Aug 15	HTMS	T	3:00	1:00	P	Q	0.672	123
J2202+4216.....	BL Lac	vs01q	1997 Dec 08	lms	T	5:15	4:30	S	B	0.069	123457
J2212+2355.....	2209+236	vs06l	1998 May 27	XGH	R	1:30	1:30	P	Q*	...	
J2225−0457.....	3C 446	vs01s	2000 Dec 02	CHS	T	5:30	3:45	P	Q	1.404	123
J2229−0832.....	2227−088	vs04i	1997 Nov 27	HTKMS	RT	6:45	3:15	P	Q	1.562	1234
J2253+1608.....	3C 454.3	vs01d	1997 Dec 12	nps	N	1:15	1:15	S	Q	0.859	123
J2320+0513.....	2318+049	vs09p	2000 Dec 08	CHMNS	NRT	7:30	5:30	P	Q	0.623	1234
J2329−4730.....	2326−477	vs04t	1998 Jun 19	HM	R	4:30	3:30	P	Q	1.306	
J2331−1556.....	2329−162	vs06b	1998 Jun 11	HTK	GU	3:30	2:00	P	Q	1.153	124
J2348−1631.....	2345−167	vs03b	1998 Jun 08	TU	G	4:00	3:30	P	Q	0.576	123

Notes.—Col. (4): Starting date of the observation Col. (5): Ground radio telescopes to which fringes were successfully obtained. Lower case letters indicate VLBA GRTs: (b) Brewster, (f) Fort Davis, (h) Hancock, (k) Kitt Peak, (l) Los Alamos, (m) Mauna Kea, (n) North Liberty, (o) Owens Valley, (p) Pie Town, (s) St. Croix. Uppercase letters indicate other GRTs: (X) Arecibo, (A) ATCA, (C) Ceduna, (E) Effelsburg, (G) Green Bank 140′, (H) Hartebeesthoek, (T) Hobart, (J) Jodrell Bank MKII, (R) Kalyazin, (K) Kashima, (N) Noto, (M) Mopra, (O) Onsala, (S) Sheshan, (P) Torun, (U) Usuda, (Y) VLA. Col. (6): Tracking Stations to which fringes were successfully obtained: (G) Goldstone, (N) Green Bank, (R) Robledo, (T) Tidbinbilla, (U) Usuda. Col. (7): Approximate time on source over which fringes were found. Col. (8): Approximate time on source over which fringes were found on space baselines. Col. (9): Correlator: (M) Mitaka, (P) Penticton, (S) Socorro. Col. (10): Optical classification: (Q) quasar, (B) BL Lac object, (G) AGNs other than B and Q (e.g., Seyfert galaxy), (E) empty field or unidentified optical counterpart; from Véron-Cetty & Véron (2001) unless appended by an asterisk (*), whereby the reference is given in the individual source notes. Col. (11): Redshift; from Véron-Cetty & Véron (2001) unless appended by an asterisk (*), whereby the reference is given in the source notes. Table 1 is also available in machine-readable form in the electronic edition of the *Astrophysical Journal Supplement*.

References.—(1) VLBApls (Fomalont et al. 2000a), http://www.aoc.nrao.edu/vlba/html/6CM/index.htm; (2) USNO (Fey et al. 1996; Fey & Charlot 1997, 2000), http://rorf.usno.navy.mil/RRFID; (3) VLBA2cm1 (Kellermann et al. 1998; Zensus et al. 2002), http://www.cv.nrao.edu/2cmsurvey/maps/index.html; (4) VLBA2cm2 (L. I. Gurvits, K. I. Kellermann, E. B. Fomalont, & H. Y. Zhang 2004, in preparation); (5) VSOPPR (Lister et al. 2001); (6) VSOPsouth (Tingay et al. 2002); (7) PR (Pearson & Readhead 1988) http://astro.caltech.edu/∼tjp/cj.

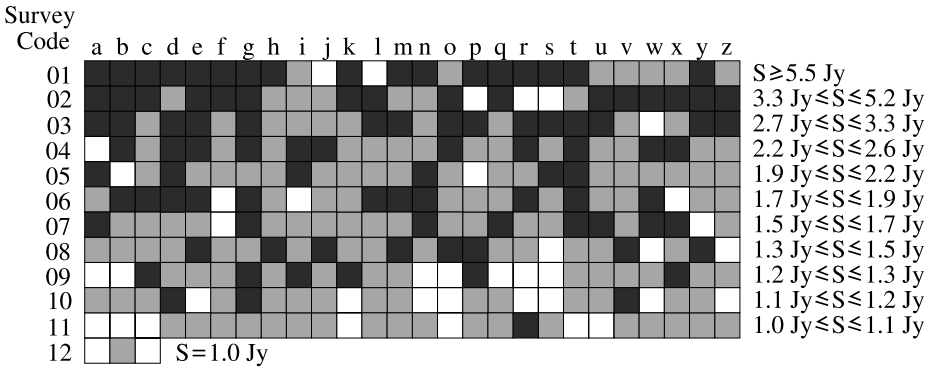

FIG. 1.—Distribution of observed sources in the VSS source list: Each experiment is denoted by its observation code, found by cross-referencing the horizontal and vertical labels. The source numbering is in decreasing order of total flux density, which is shown to the right of each line. The darker squares indicate the sources presented in this paper. The lighter shaded squares are sources observed but not yet fully reduced as of the end of 2002, or of suspect quality. Many of these have been rescheduled. The white squares are Survey sources not yet observed as of the end of 2002.

the visibility amplitudes of the 102 sources in this paper were compared with those found in the VLBApls in order to find any remaining systematic flux density offsets. We compared the flux densities we found with those from the VLBApls at nearby points on the (u, v) plane (less than 10 Mλ apart). This allows sources with significant structure to be compared directly. To take account of the high variability often seen in these sources we corrected for the change in flux density between the VLBApls and the Survey experiments by using data from the Australia Telescope Compact Array (ATCA; Tingay et al. 2003) or the University of Michigan Radio Astronomy Observatory (UMRAO)[18] monitoring programs. This variability information was available for approximately 80% of the Survey sources. This comparison is at best a zeroth-order correction, as it can only correct for the flux density changes in the object as a whole, while the individual (u, v) sample points will be affected differently by the variability.

We selected those experiments for which we had some measure of the source variability. In addition, to exclude the most extremely variable sources, we required the VLBApls and Survey visibilities to agree to within a factor of 2.5. Finally, we restricted ourselves to only comparing visibility points for which the correlated flux density on baselines to *HALCA* was greater than 0.5 Jy.

We found that the median ratio of the Survey to VLBApls correlated flux density was 0.83 with an error in the median of approximately 0.05. The origin of this discrepancy between the two surveys is not understood at this time. All the VSOP Survey visibilities have been rescaled upward by 1.2, the reciprocal of this factor. The median ratio for VLBA data extraction experiments was slightly closer to unity than for non-VLBA experiments. As the system temperatures and gain curves for the VLBA GRTs are significantly better than those from non dedicated VLBI arrays this is of no surprise. Comparing the VLBApls to ATCA monitoring data (Tingay et al. 2003), and the UMRAO database, we find that the median ratio is close to unity (1.03 with an error in the median of 0.04).

The second factor affecting the image fidelity is the uneven and often poor sampling of the (u, v) plane. The effect of uneven (u, v) sampling has been investigated by Lister et al. (2001). In simulations involving VLBA+*HALCA* (u, v) plane coverage they found that the peak value in their simulated images divided by the maximum difference between the simulated images and the original model was between approximately 30:1 to 100:1. This is probably a much better indicator of the image fidelity than the dynamic range, which was much higher for their images ($\geq$1000:1). For our images the dynamic range and image fidelity will almost certainly be less than their values, owing to the larger uncertainty often present in the relative visibility amplitude scaling, and the smaller number of baselines.

Hence, based upon the findings of Lister et al. (2001), and after applying the overall systematic error factor of 20%, we conservatively estimate that our image fidelity is in the 20:1 range, i.e., caution should be exercised when interpreting any features in the images at approximately the 5% level of the peak flux density, or less. For the images constructed from GOT data using the VLBA this figure may be higher, while for images from Survey observations using non-VLBA antennas this figure may be as low as 10:1, owing to additional uncertainty in the amplitude scaling of the GRTs.

This amplitude scaling uncertainty will also affect the peak flux densities listed for the images. The 1 σ scatter in the ratios of the Survey to VLBApls correlated flux density was approximately 0.2. A portion of this scatter will be due to source variability, for which we only made a single, global correction for each experiment. However, if we assume that all the scatter is simply due to errors in the visibility amplitudes, then this gives us a conservative error estimate. The errors in the peak flux values for each image will be comparable, i.e., approximately 20%.

3.2. *Model-Fitting and Brightness Temperature Determination*

After obtaining the best image of a source the visibilities were model-fitted with Difmap to a small number of components, typically a combination of two or three δ-functions, circular Gaussians, or elliptical Gaussians. The precise number and type of components were chosen to minimize the χ^2, while at the same time keeping the number of free parameters as small as possible. Minimizing the number of components (i.e., model-fitting to only the strongest components) also helps to reduce the possibility of model-fitting a component that is not, in fact, real. In almost all cases the integrated flux of any weaker components in a source was greater than 5% of the integrated flux of the strongest component. The only exceptions were for sources J1229+0203 and J1407+2827. In both of these cases a weak, point-source component was necessary to fit the visibilities on the longer baselines.

[18] See http://www.astro.lsa.umich.edu/obs/radiotel/umrao.html.

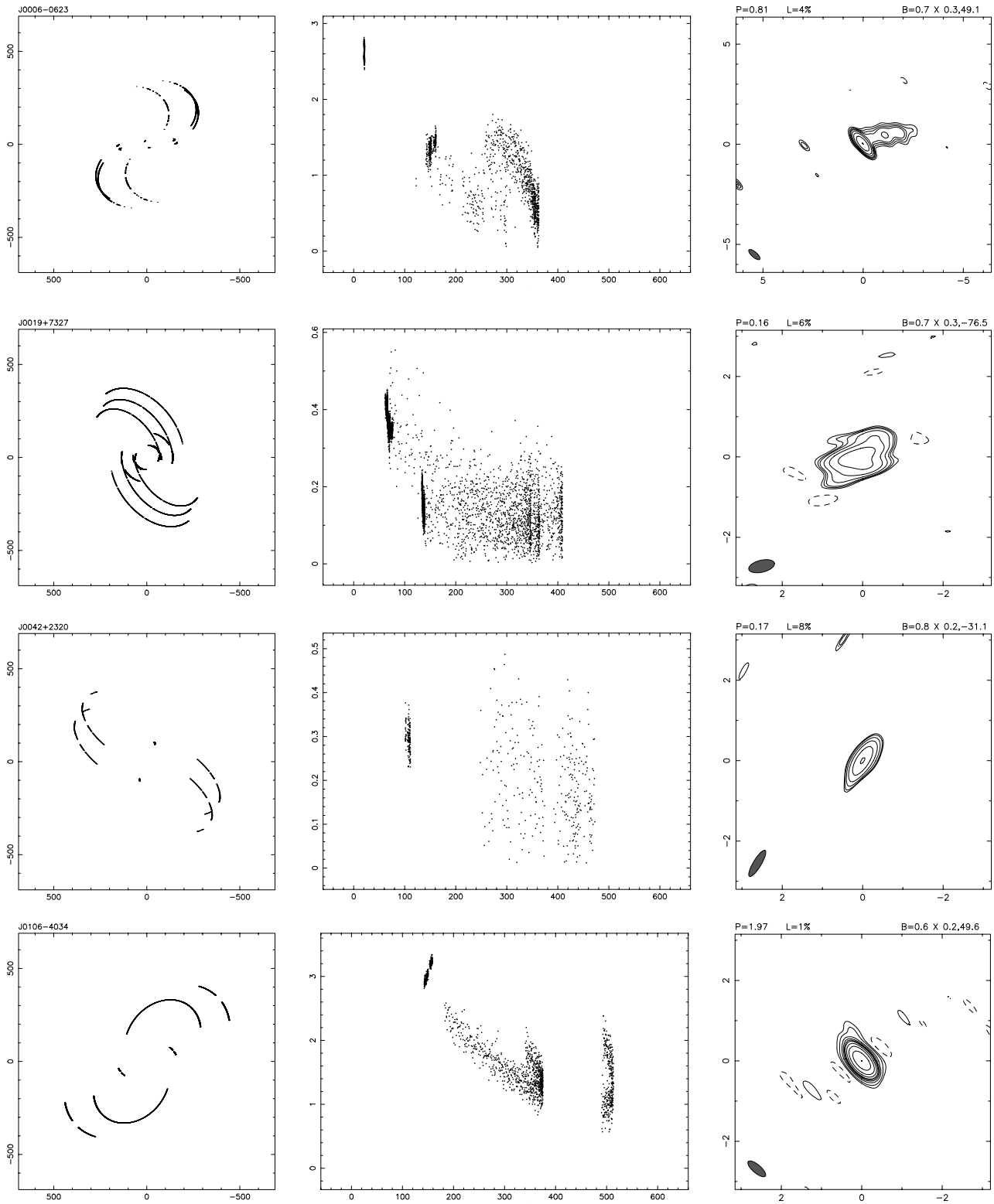

FIG. 2.—Images of the Survey sources: For each source three separate panels are presented horizontally across the page. The first panel shows a plot of the (u, v) coverage, with u on the horizontal axis and v on the vertical axis. Both axes are measured in units of Mλ. The second panel shows a plot of the amplitude of the visibilities (in janskys) vs. (u, v) radius, with the latter again measured in Mλ. For both of these plots only data that were actually used to make the final image are shown. Finally, a contour plot of the cleaned image is shown on the right. The contour levels are expressed as a percentage of the peak flux density and have the following pattern: 0.5%, 1%, 2%, 4%, 6%, 8%, 10%, 15%, 25%, 50%, and 99%, along with an additional negative contour, equal in magnitude to the minimum positive contour level. The peak flux density in mJy, minimum contour level, and synthesized HPBW in milliarcsec are shown on the top border.

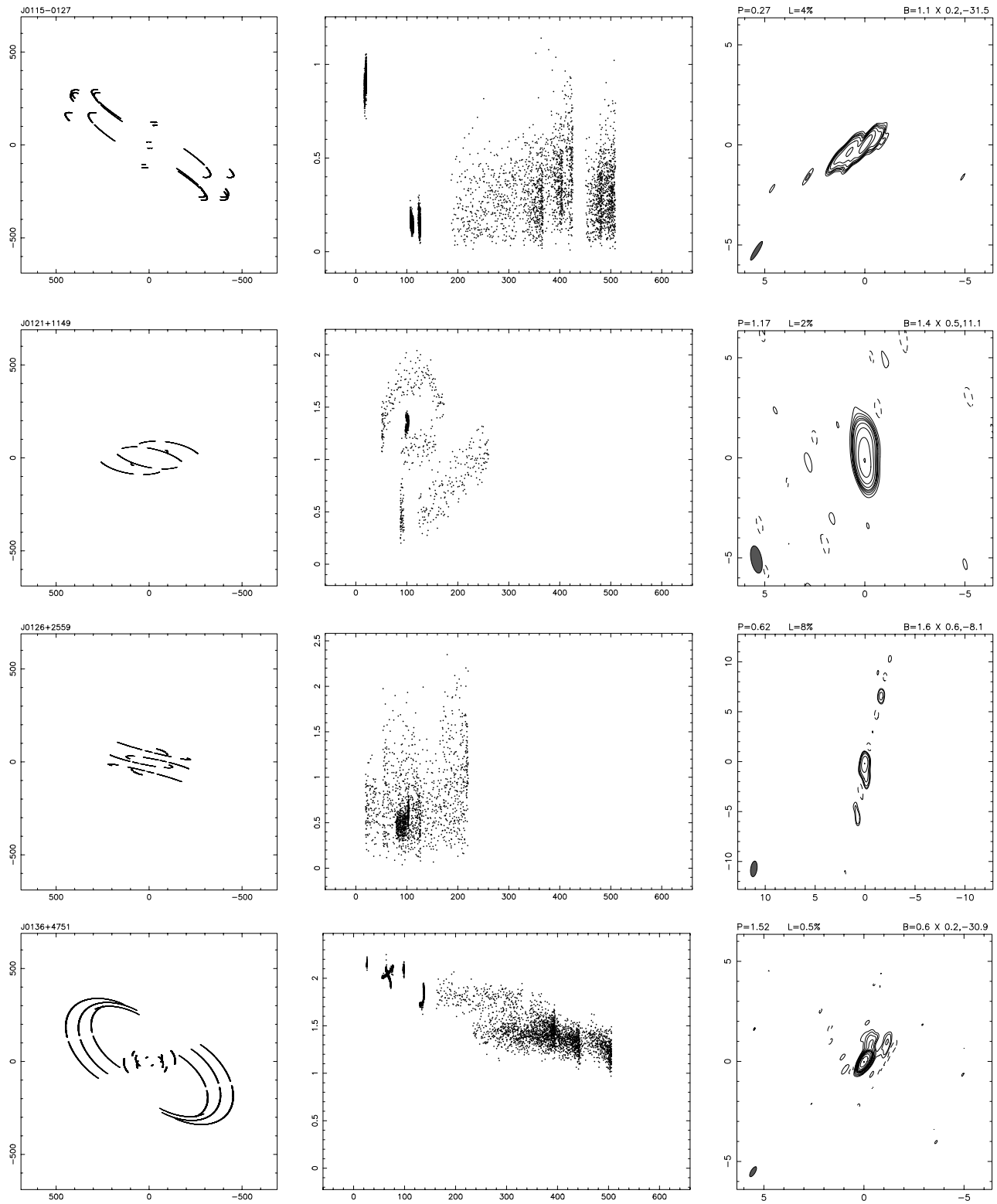

FIG. 2.—*Continued*

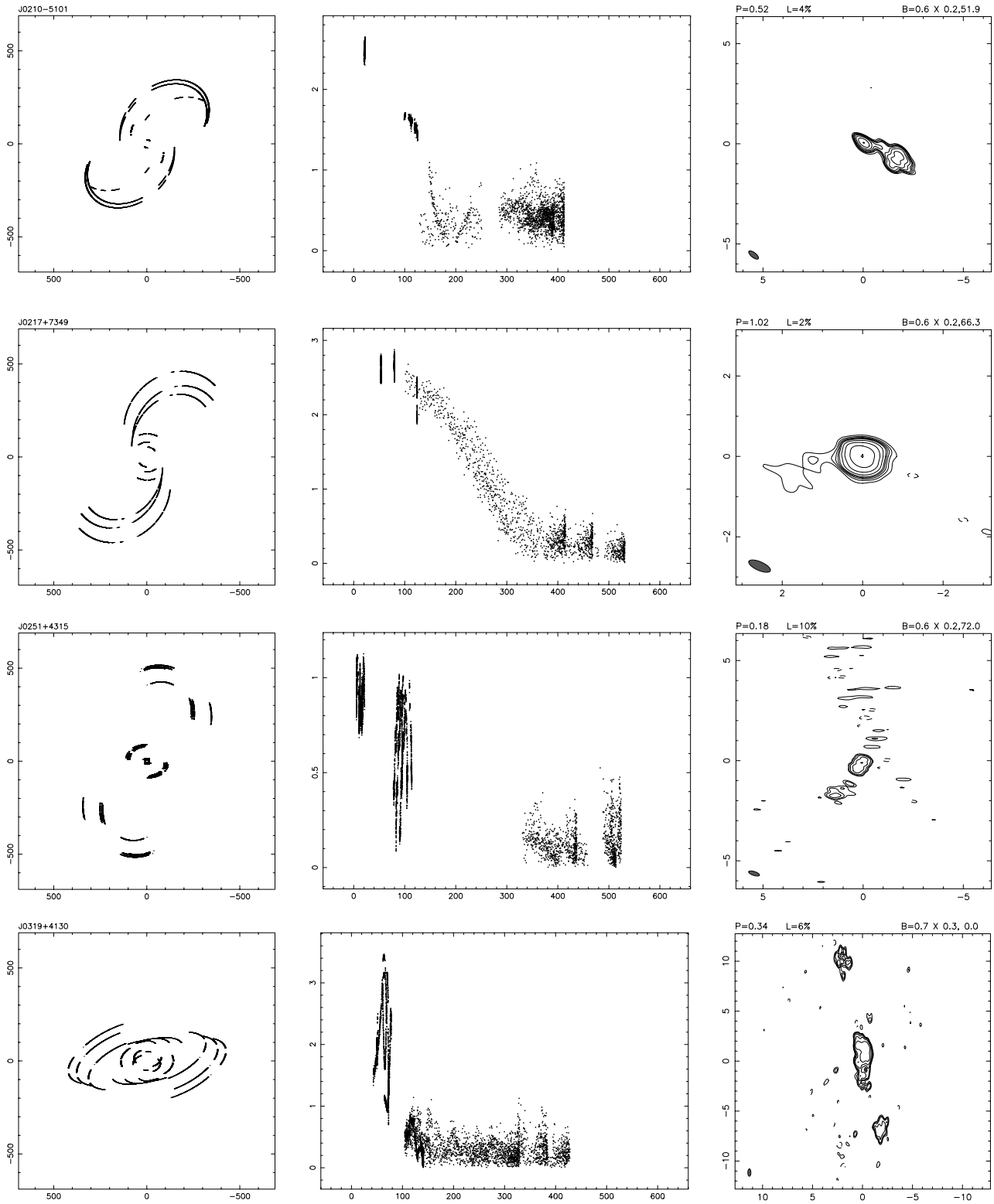

FIG. 2.—*Continued*

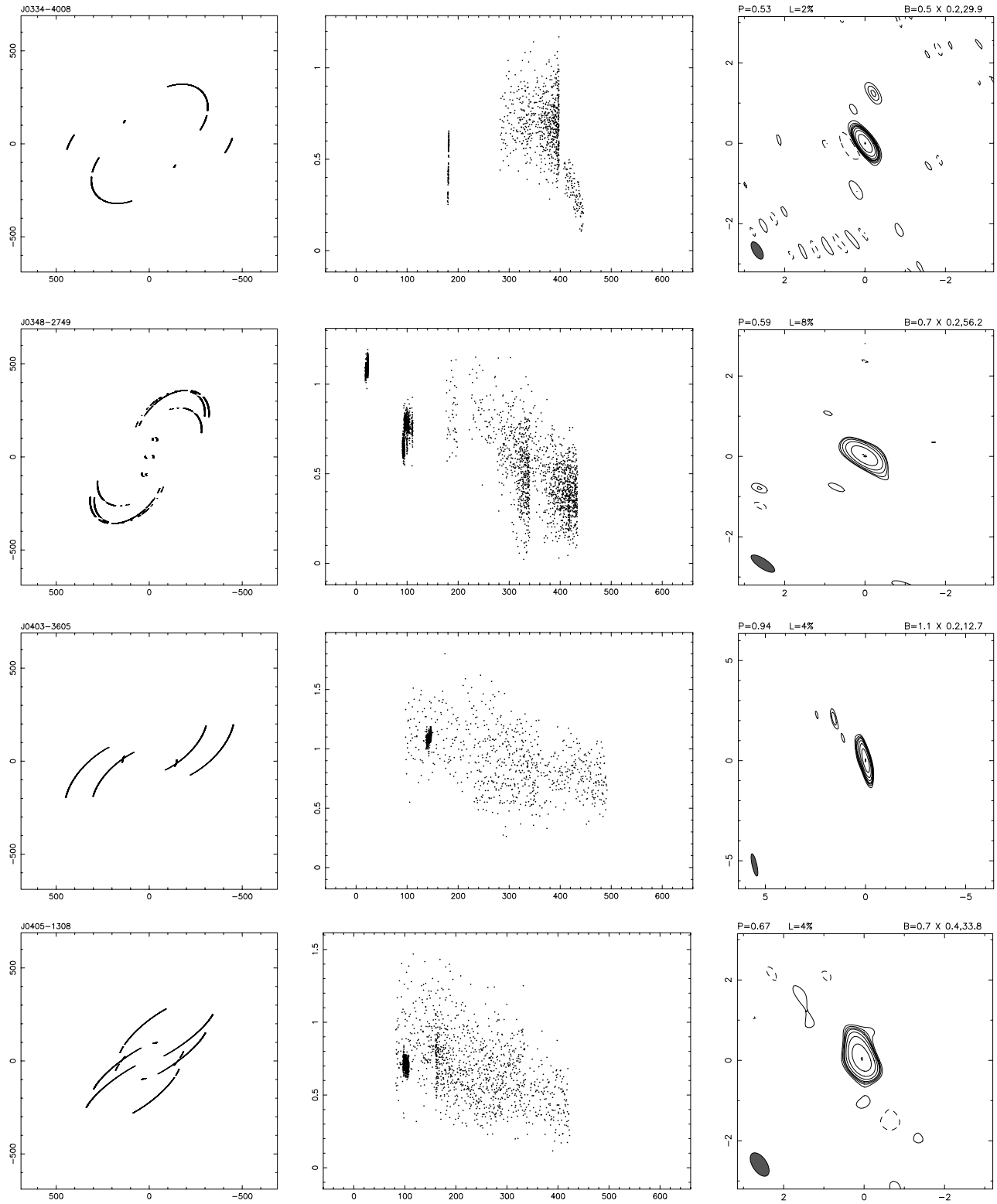

FIG. 2.—*Continued*

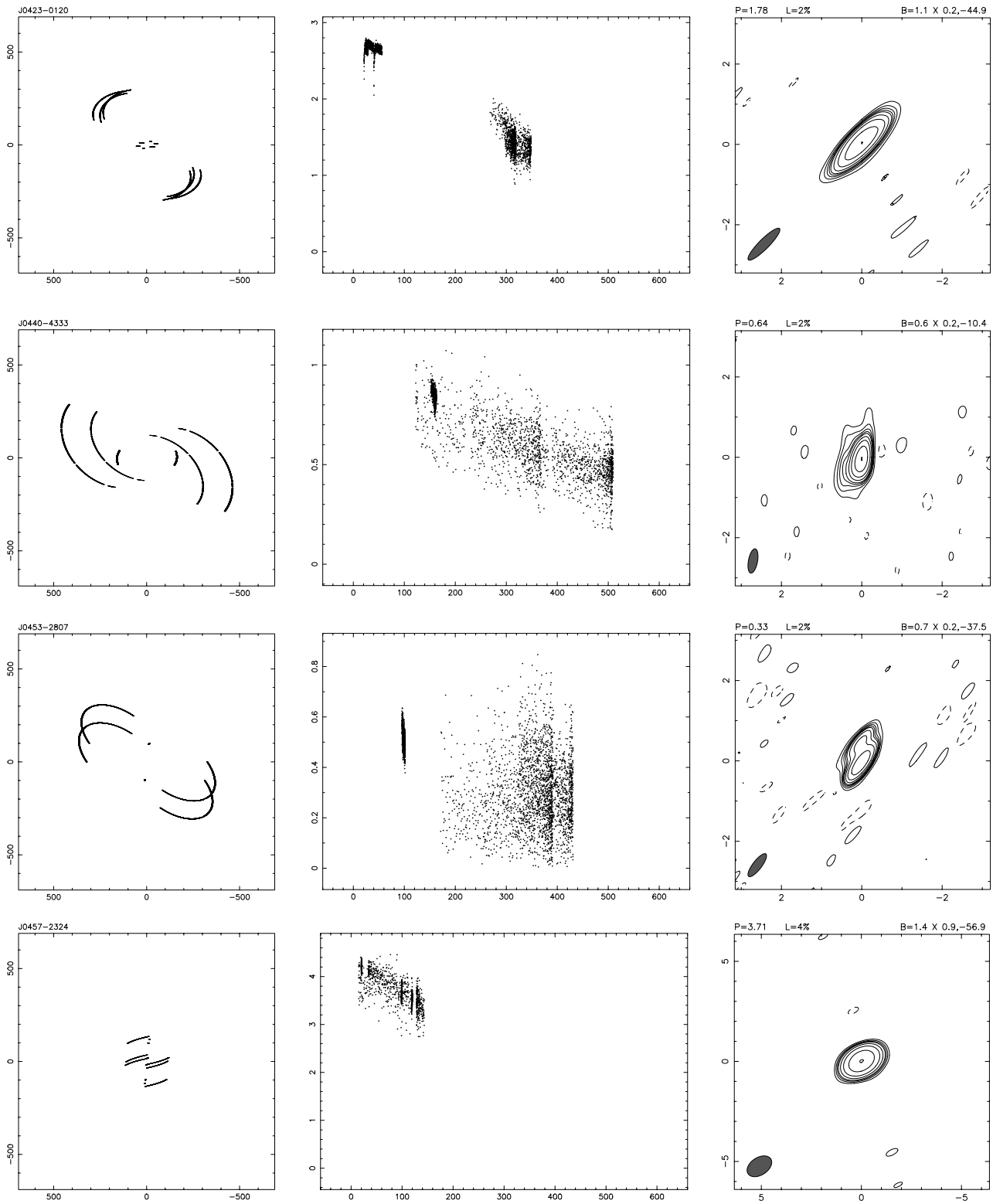

FIG. 2.—*Continued*

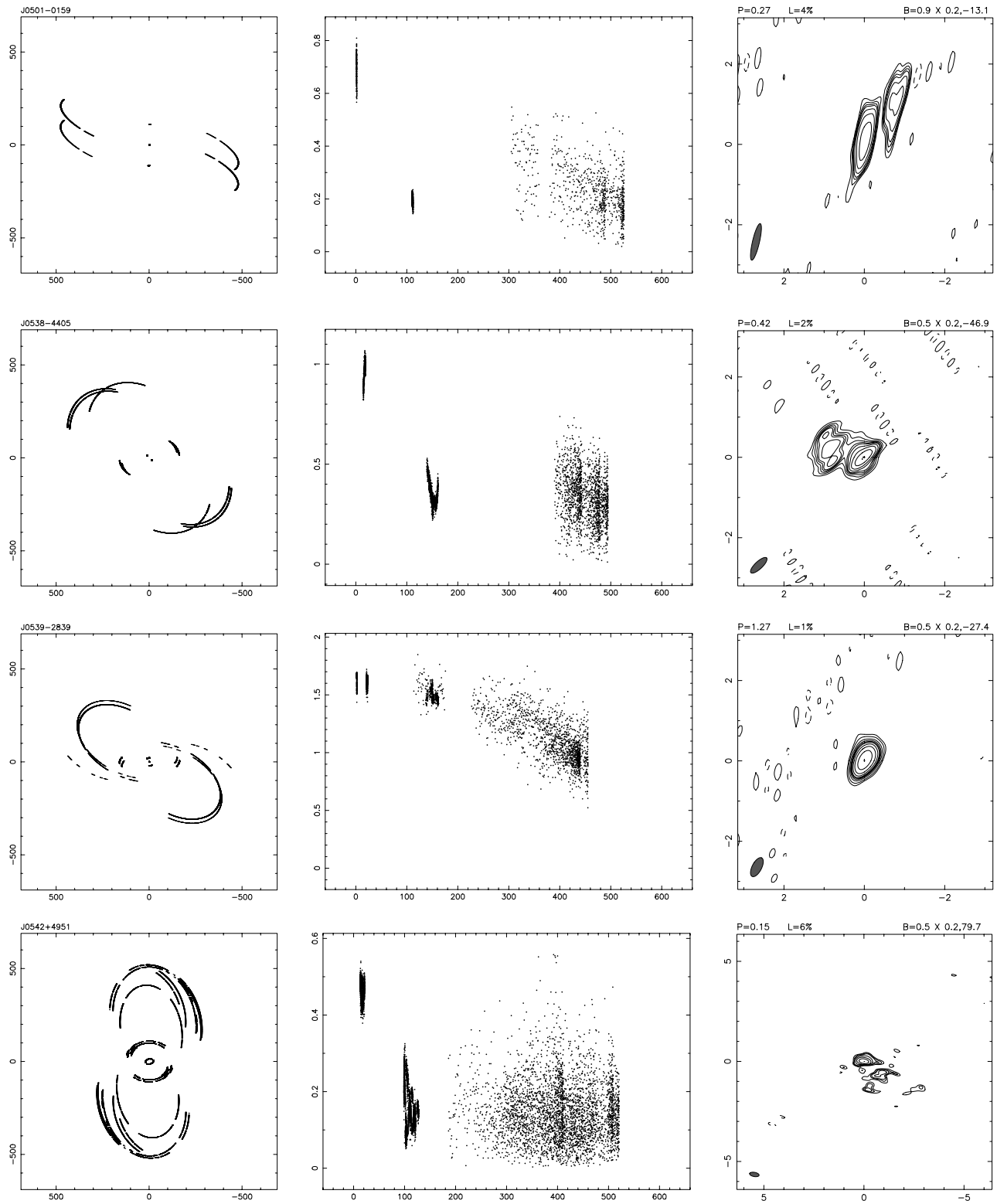

FIG. 2.—*Continued*

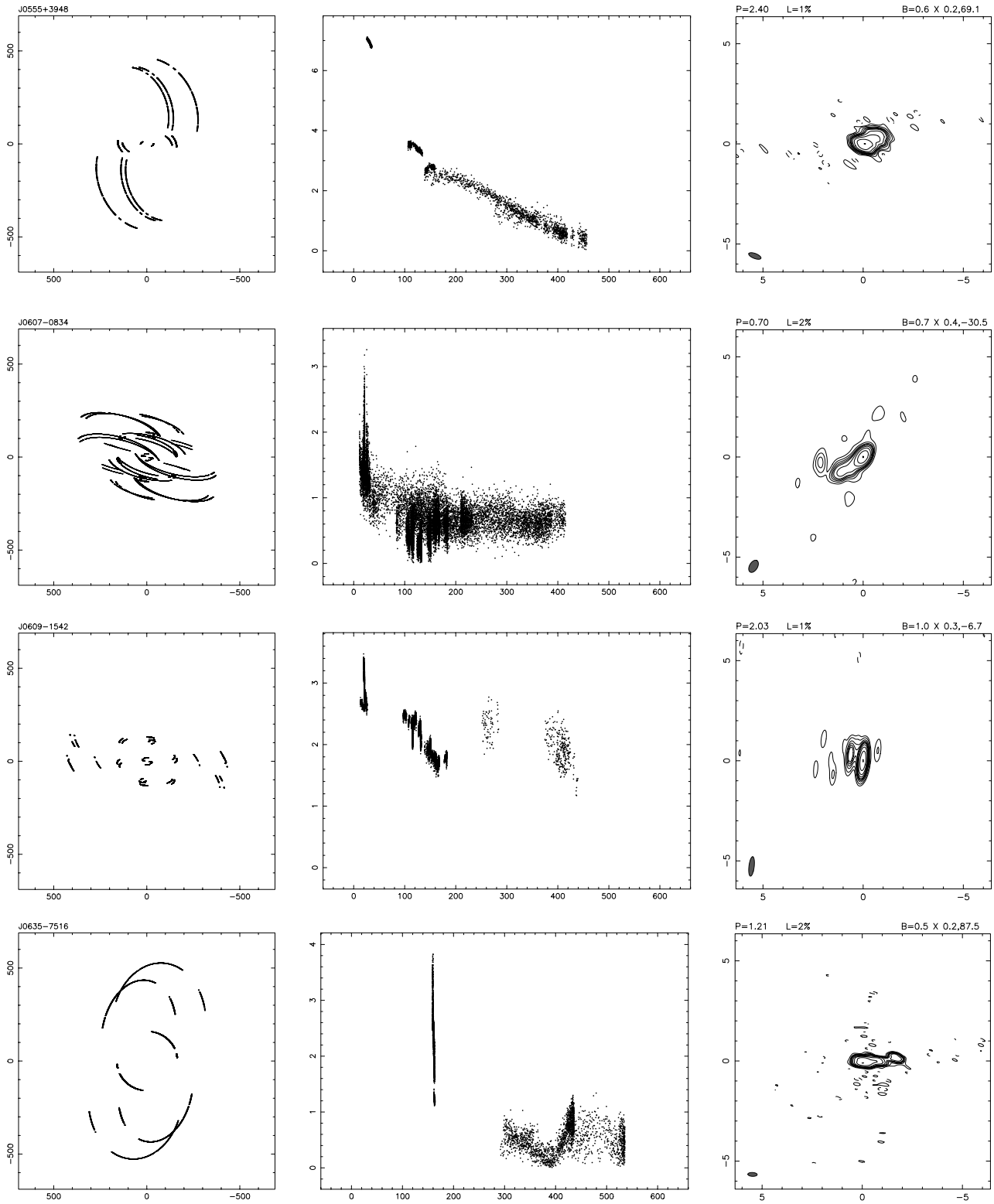

FIG. 2.—*Continued*

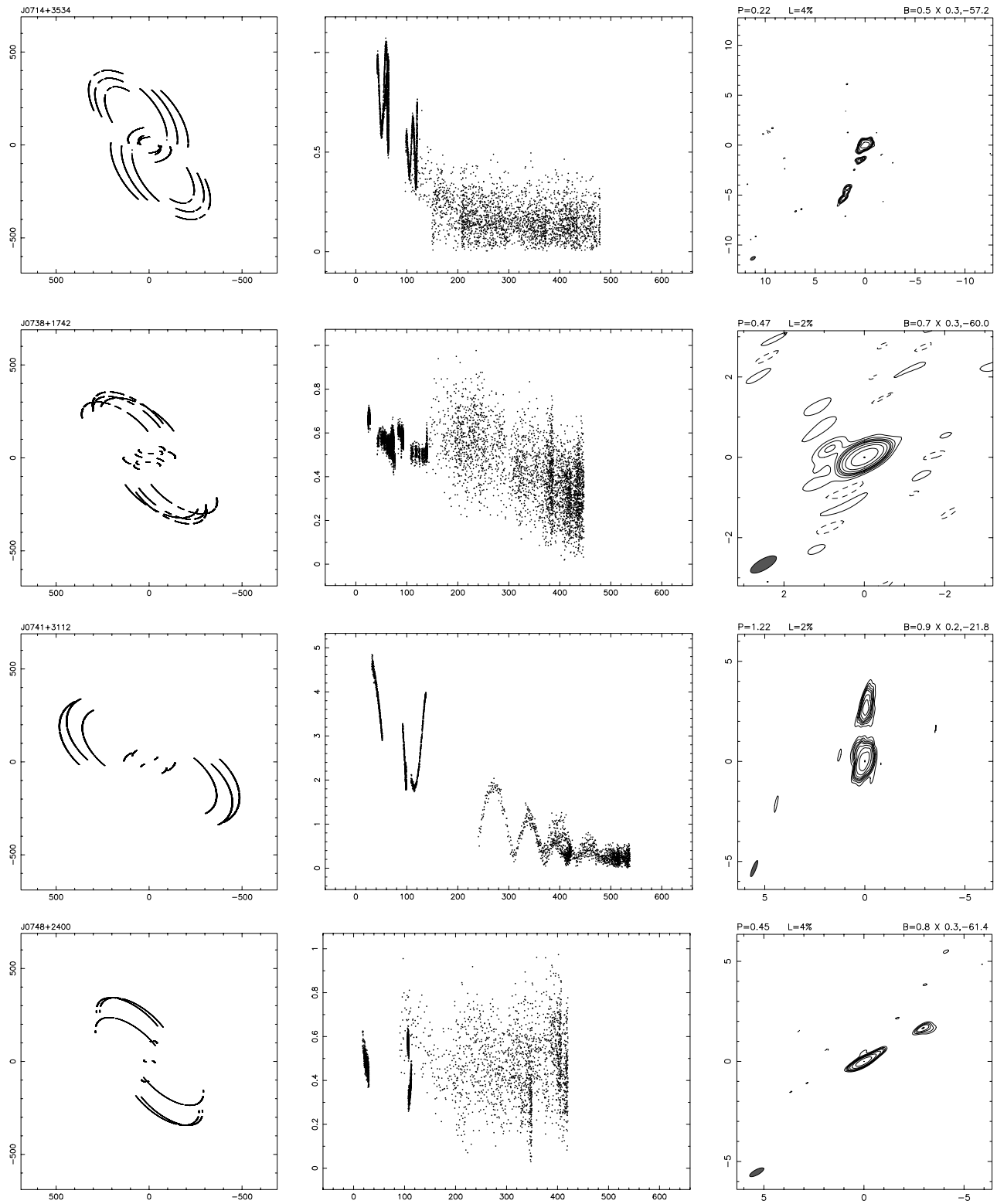

FIG. 2.—*Continued*

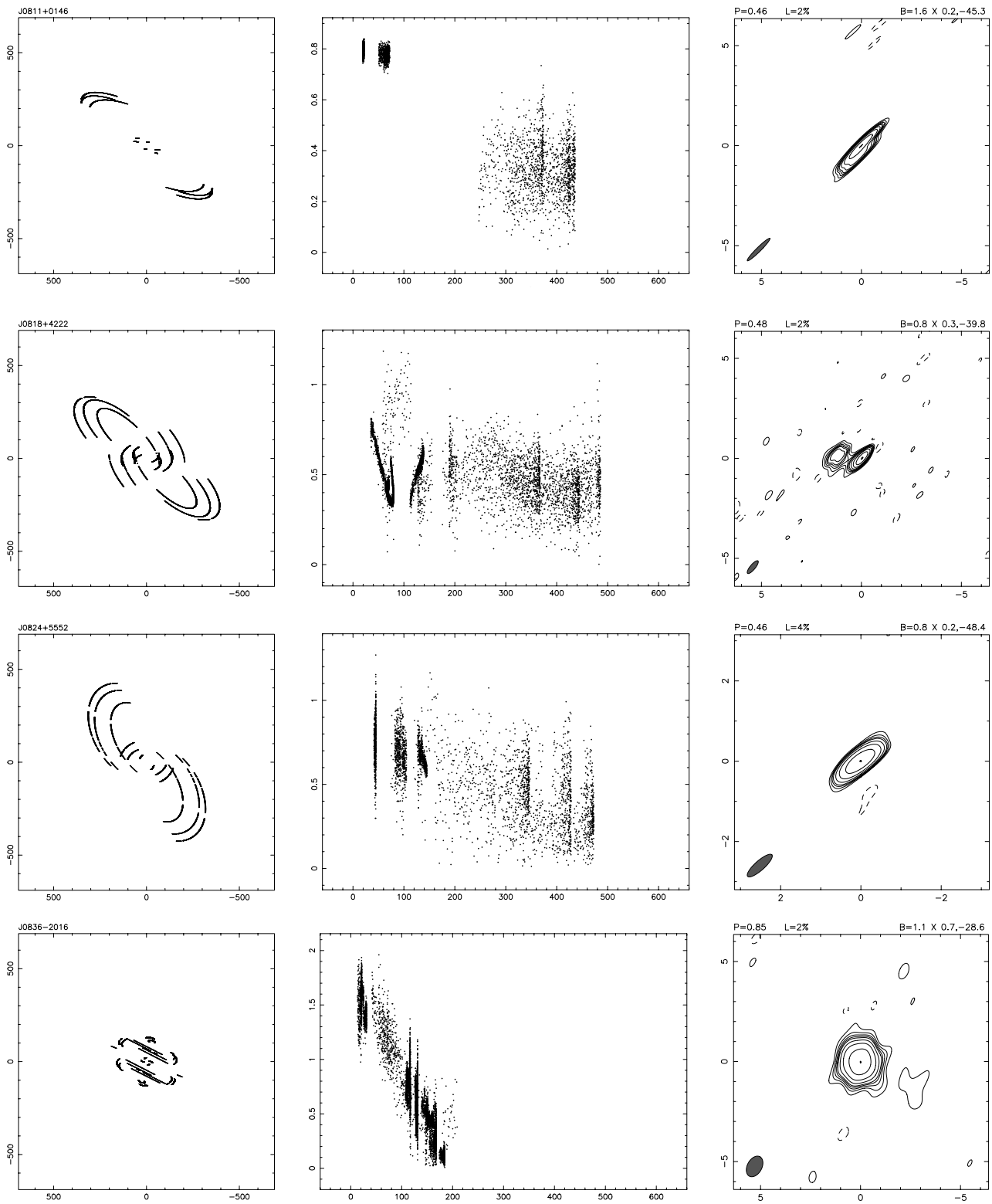

FIG. 2.—*Continued*

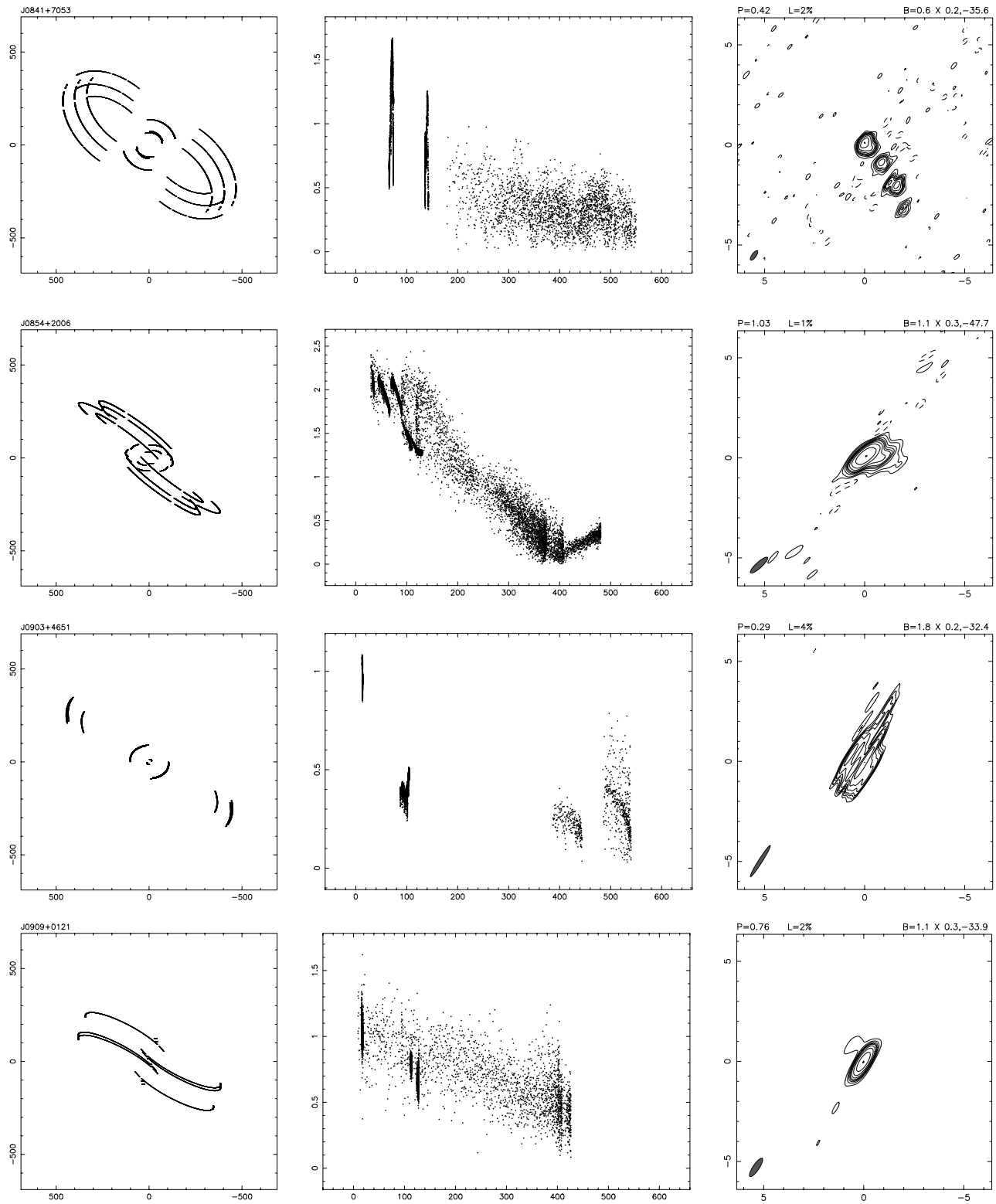

FIG. 2.—*Continued*

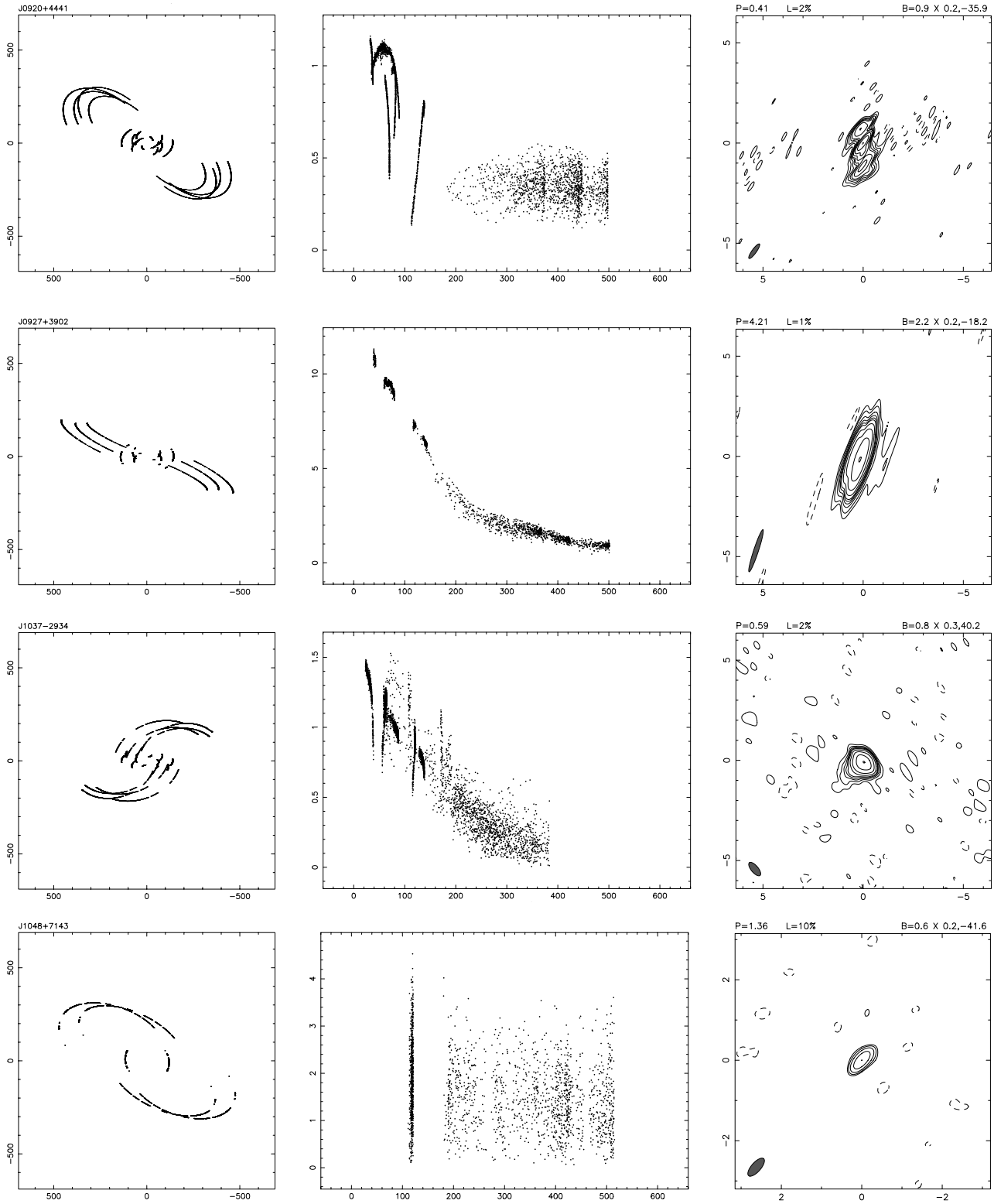

FIG. 2.—*Continued*

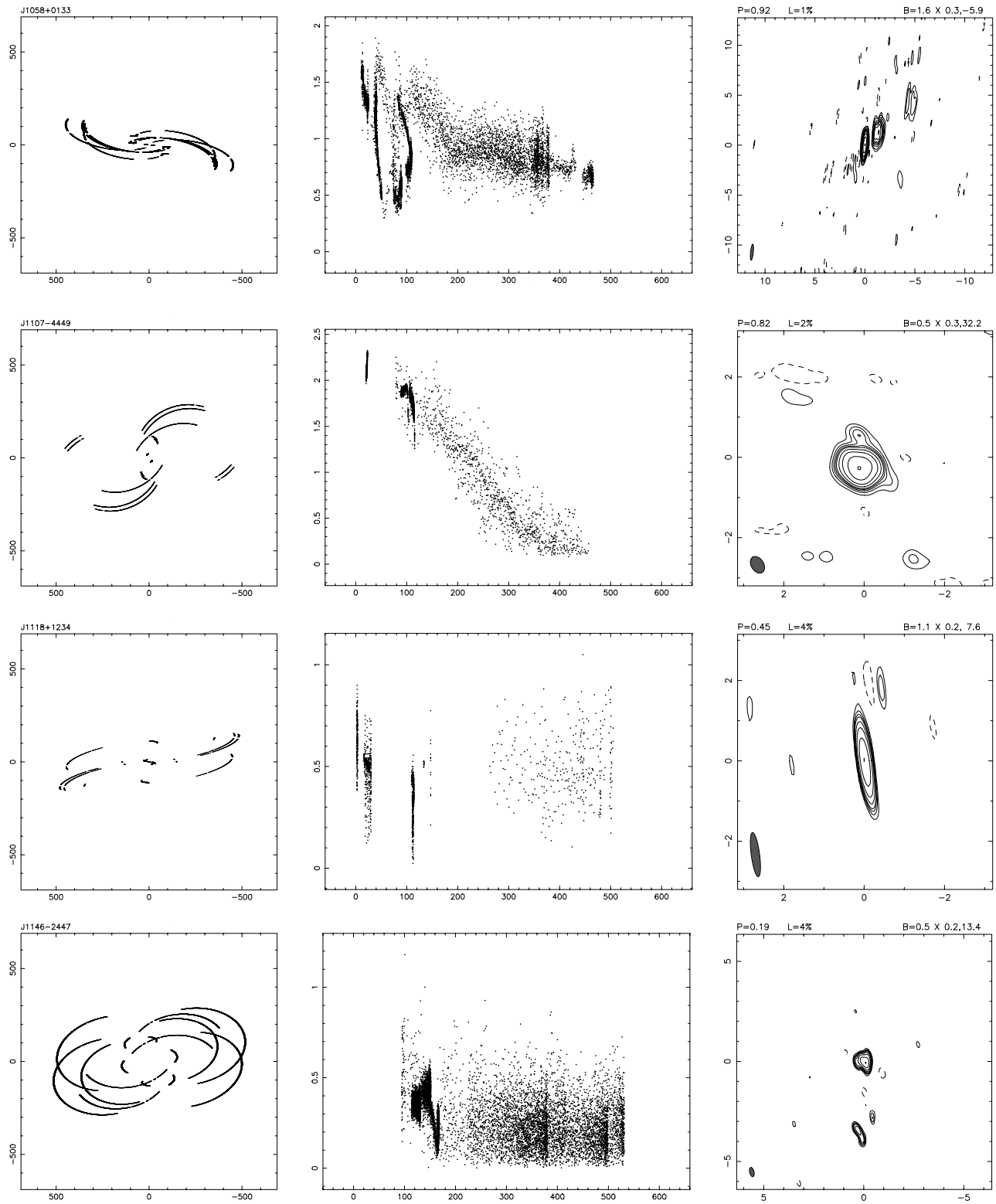

FIG. 2.—*Continued*

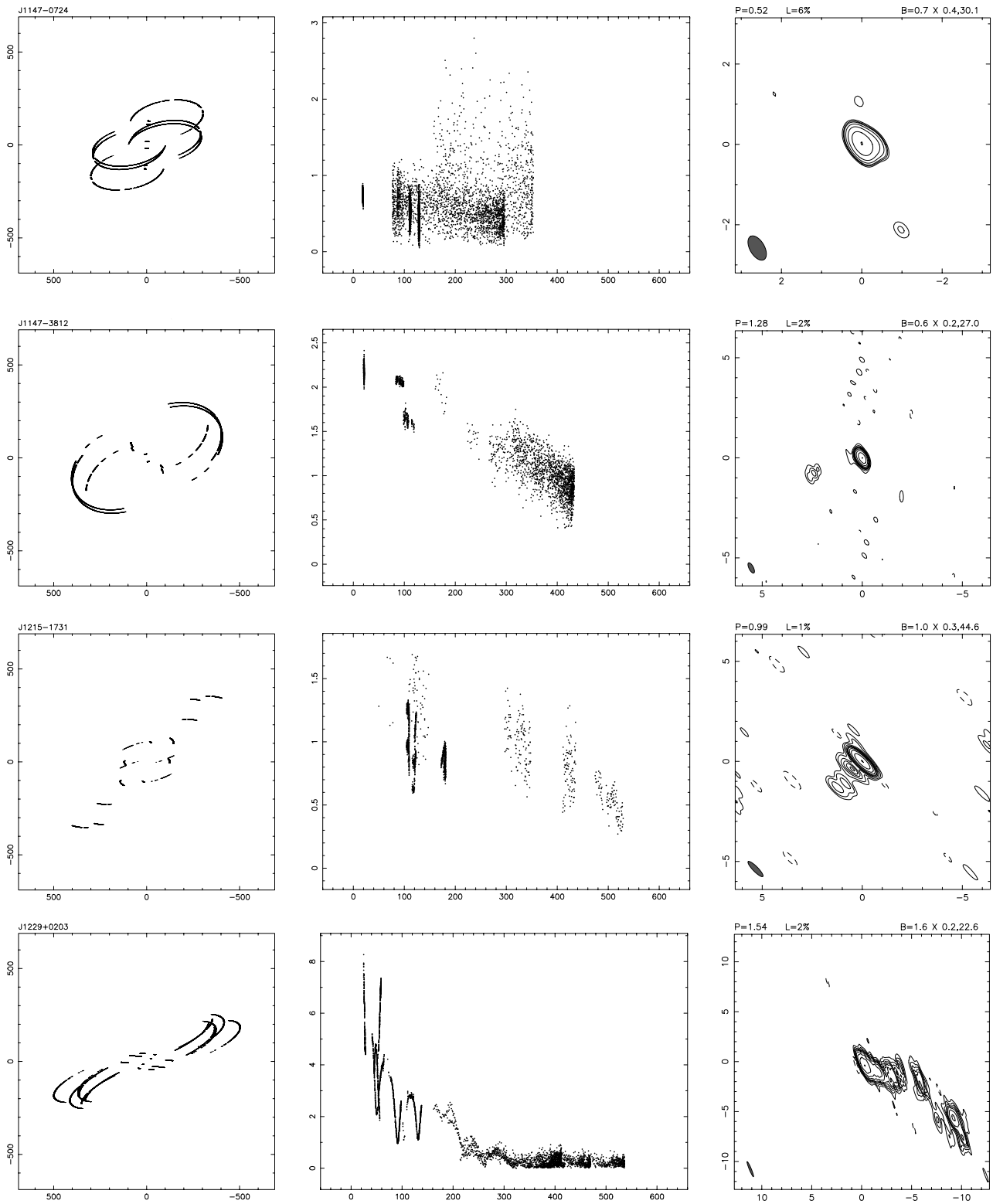

FIG. 2.—*Continued*

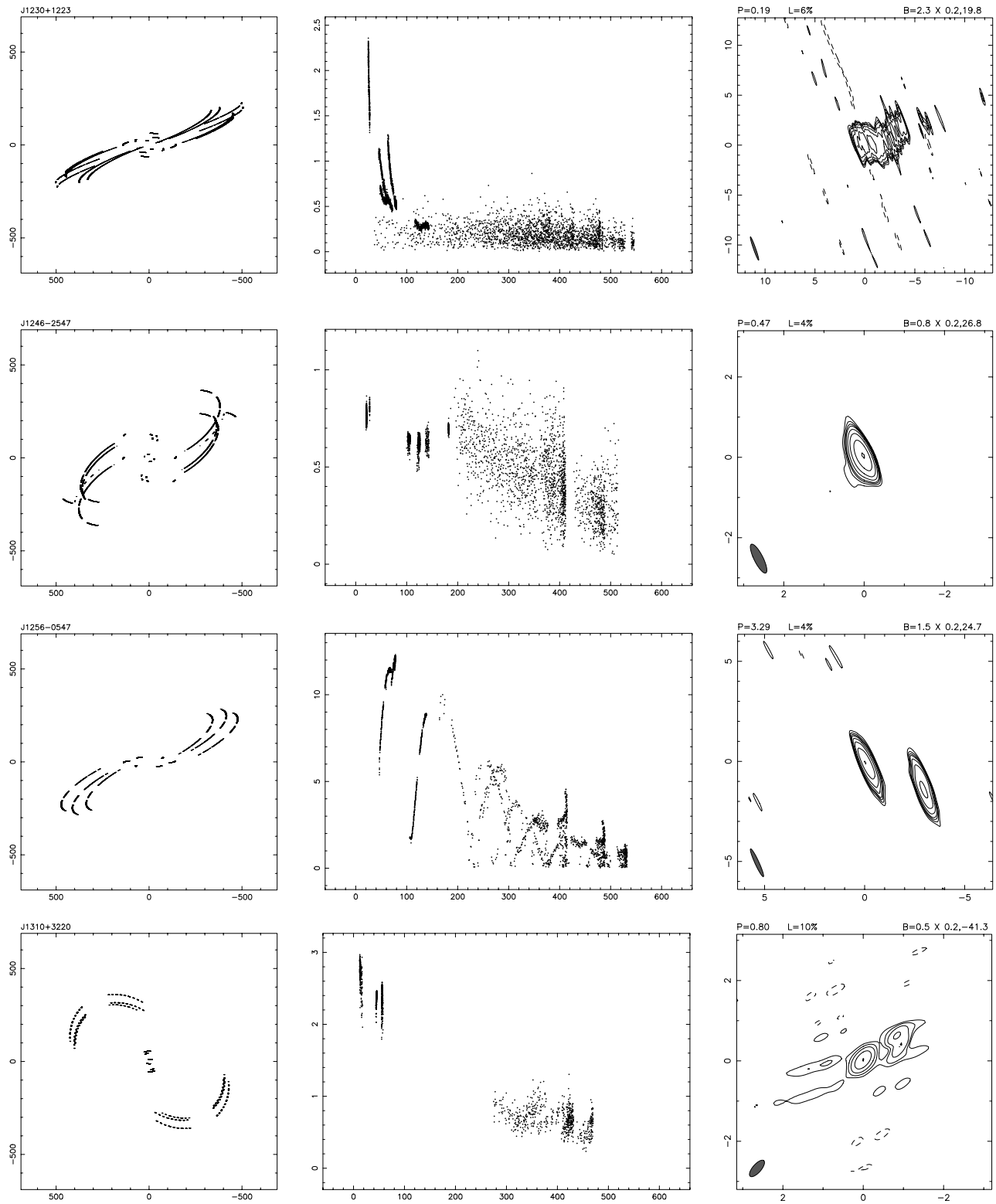

FIG. 2.—*Continued*

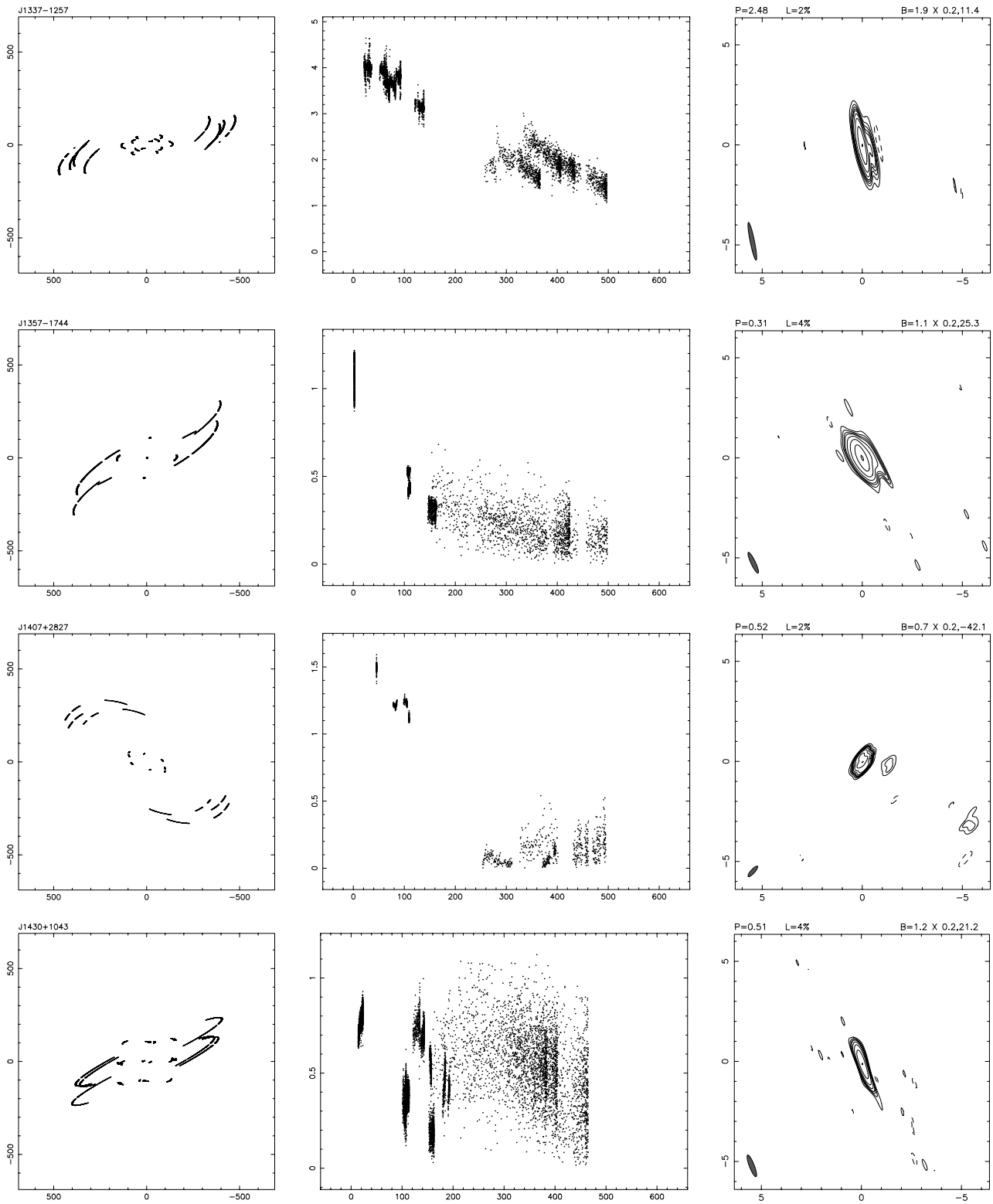

FIG. 2.—*Continued*

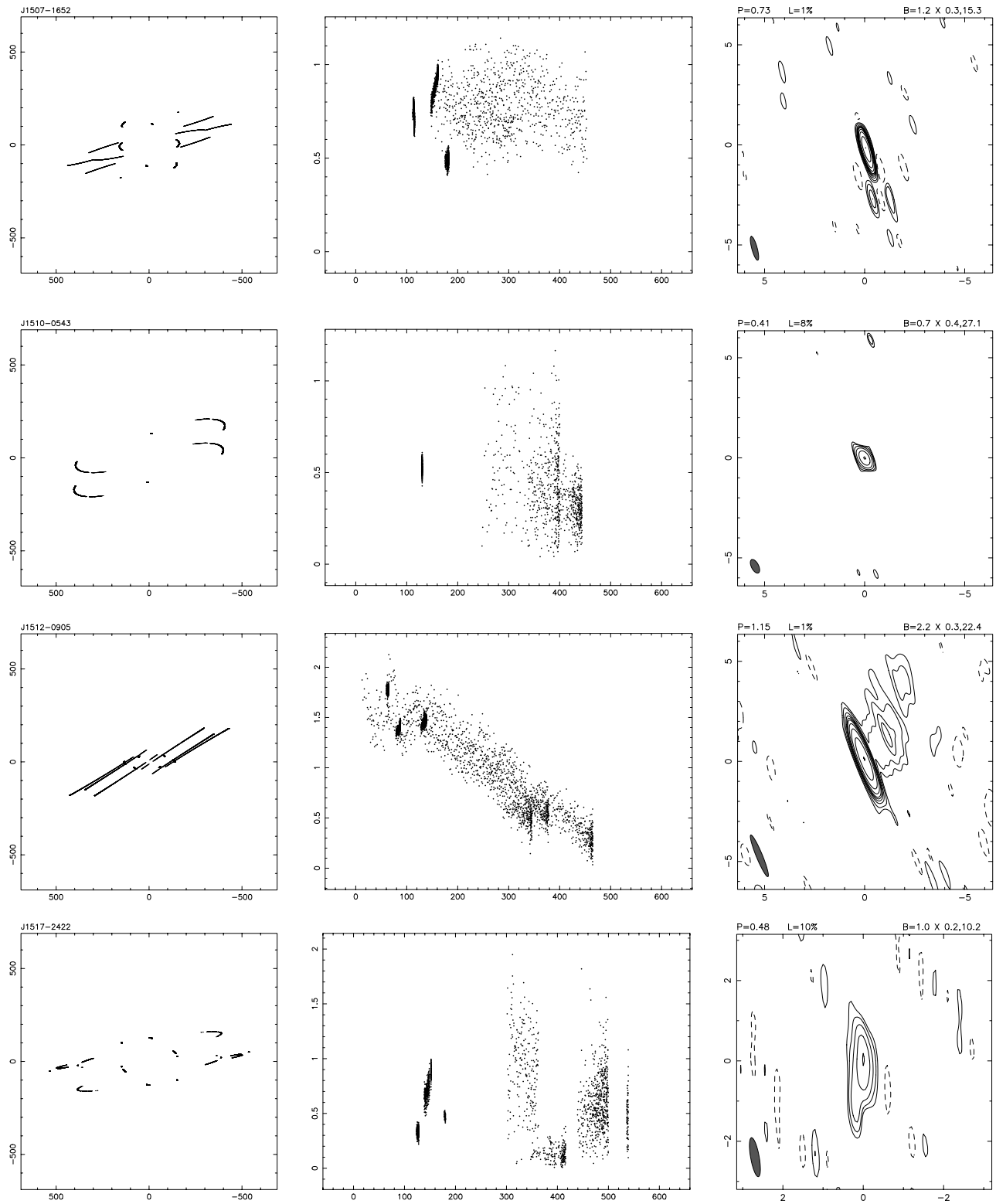

FIG. 2.—*Continued*

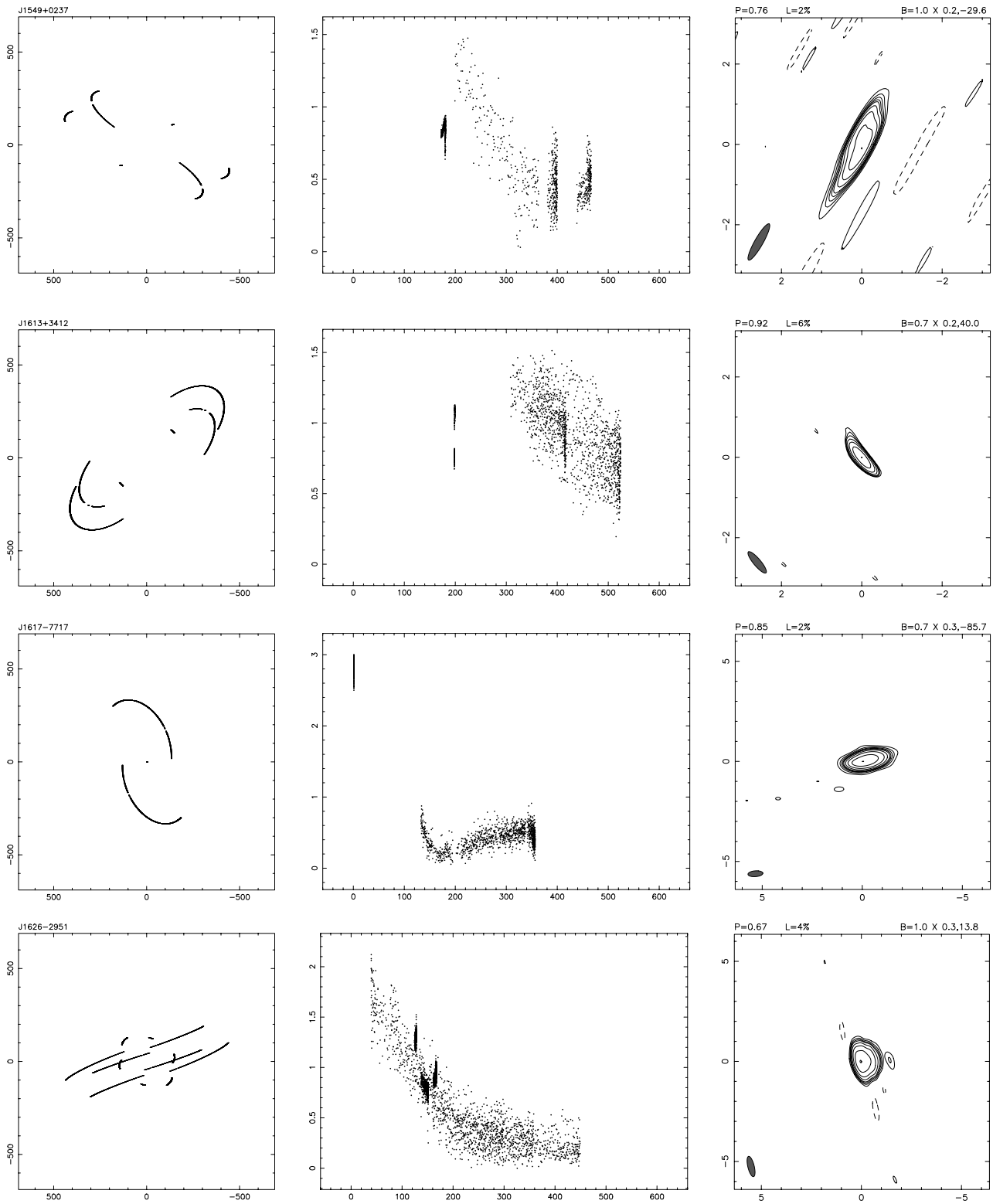

FIG. 2.—*Continued*

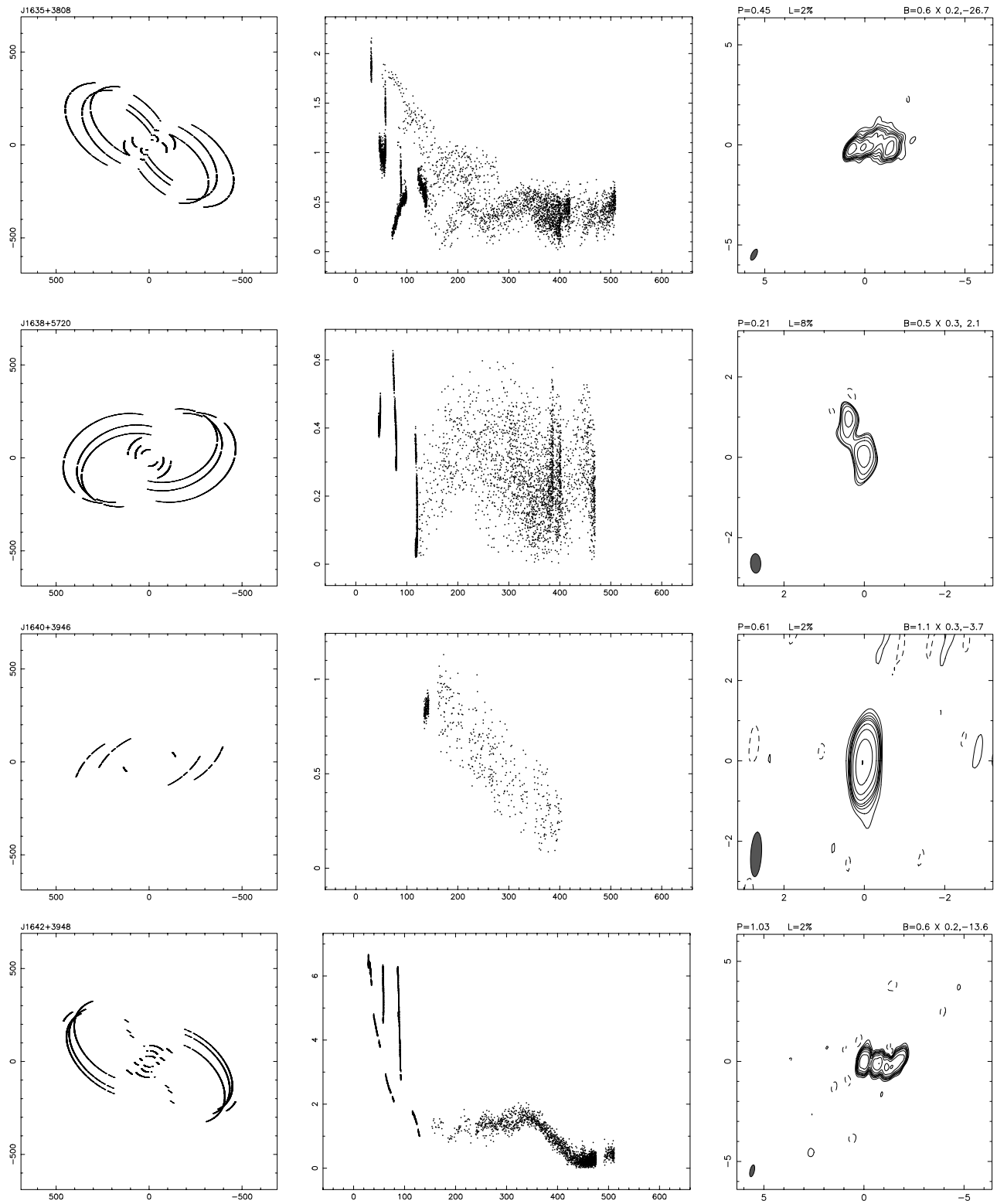

FIG. 2.—*Continued*

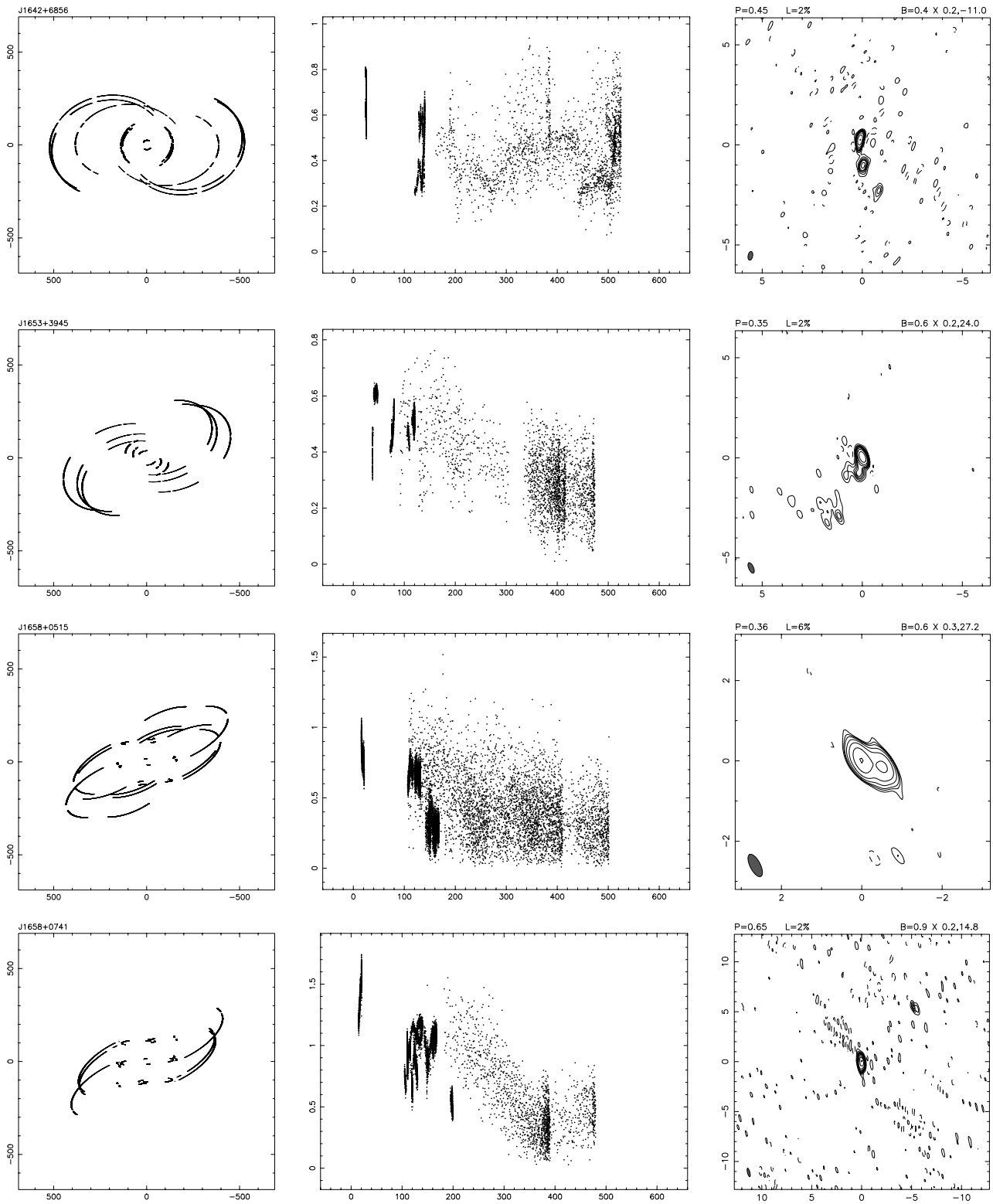

FIG. 2.—*Continued*

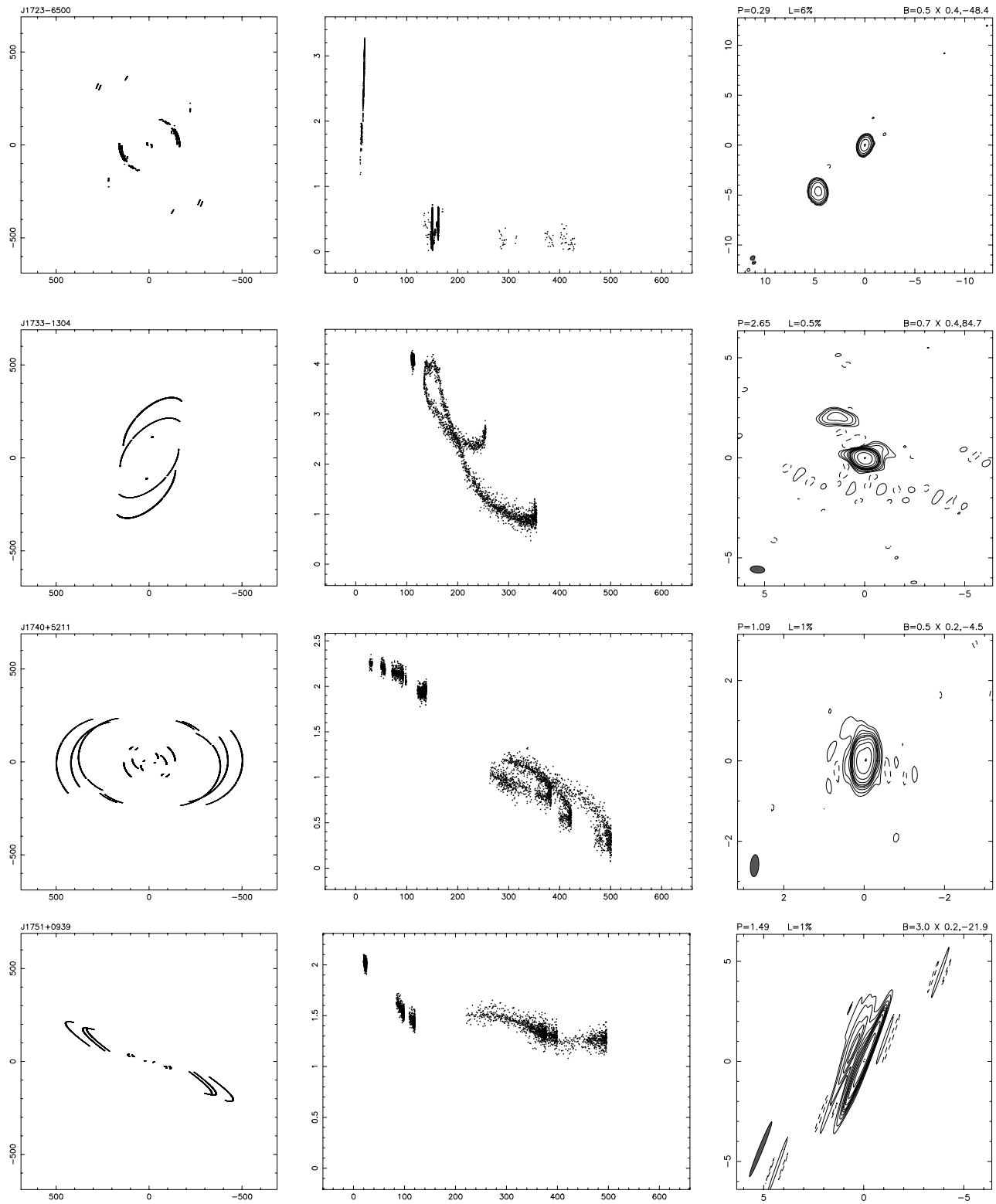

FIG. 2.—*Continued*

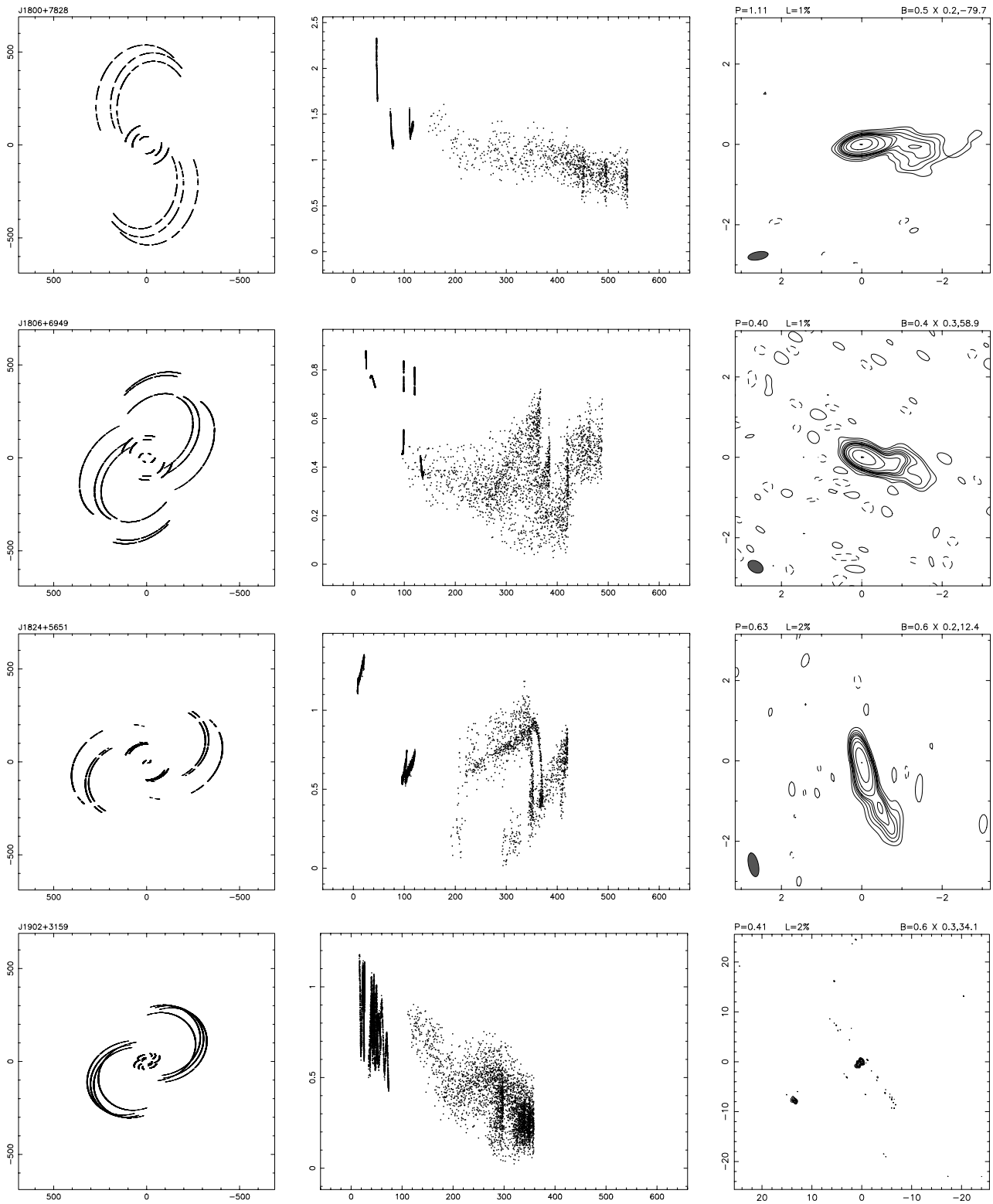

FIG. 2.—*Continued*

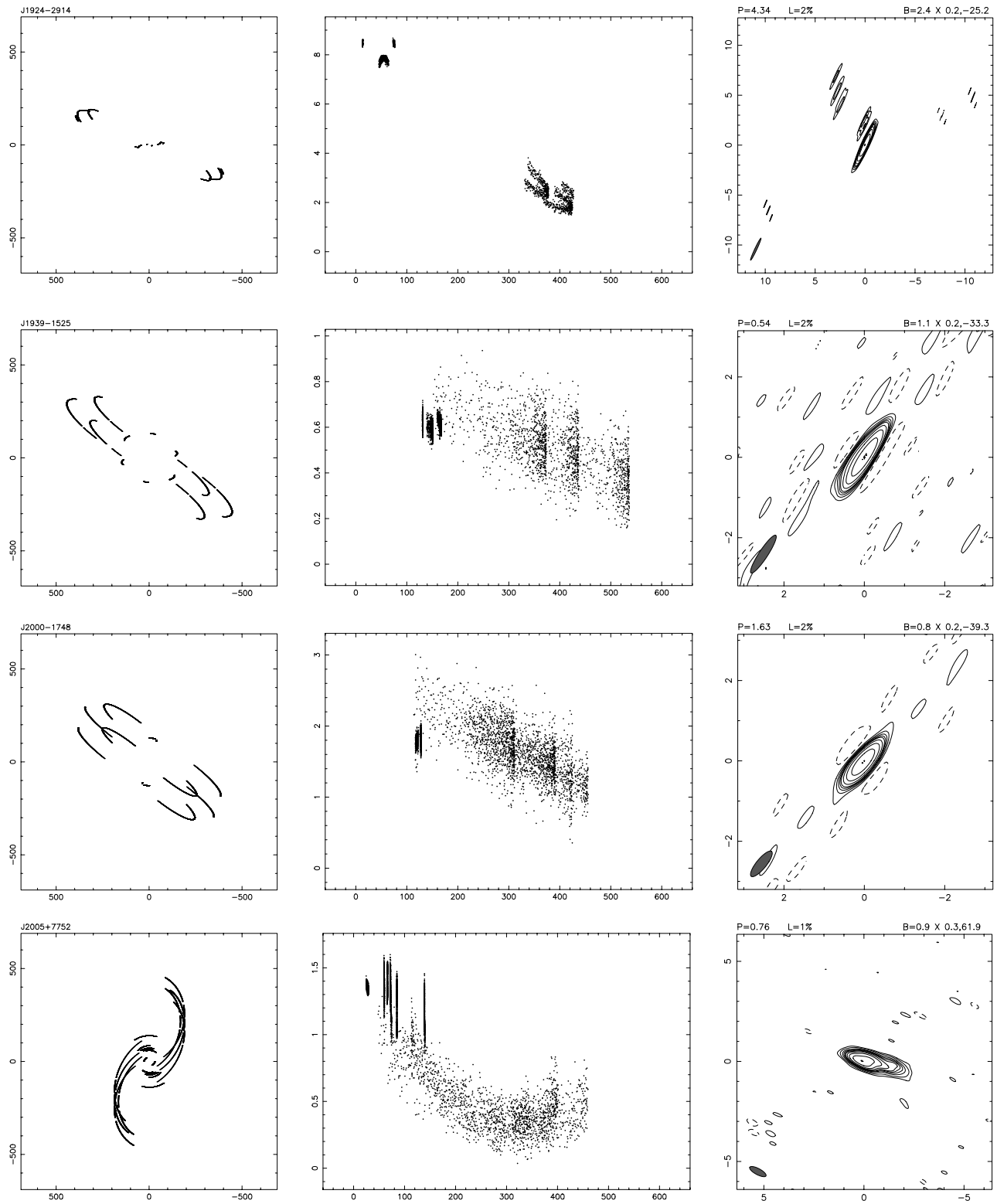

FIG. 2.—*Continued*

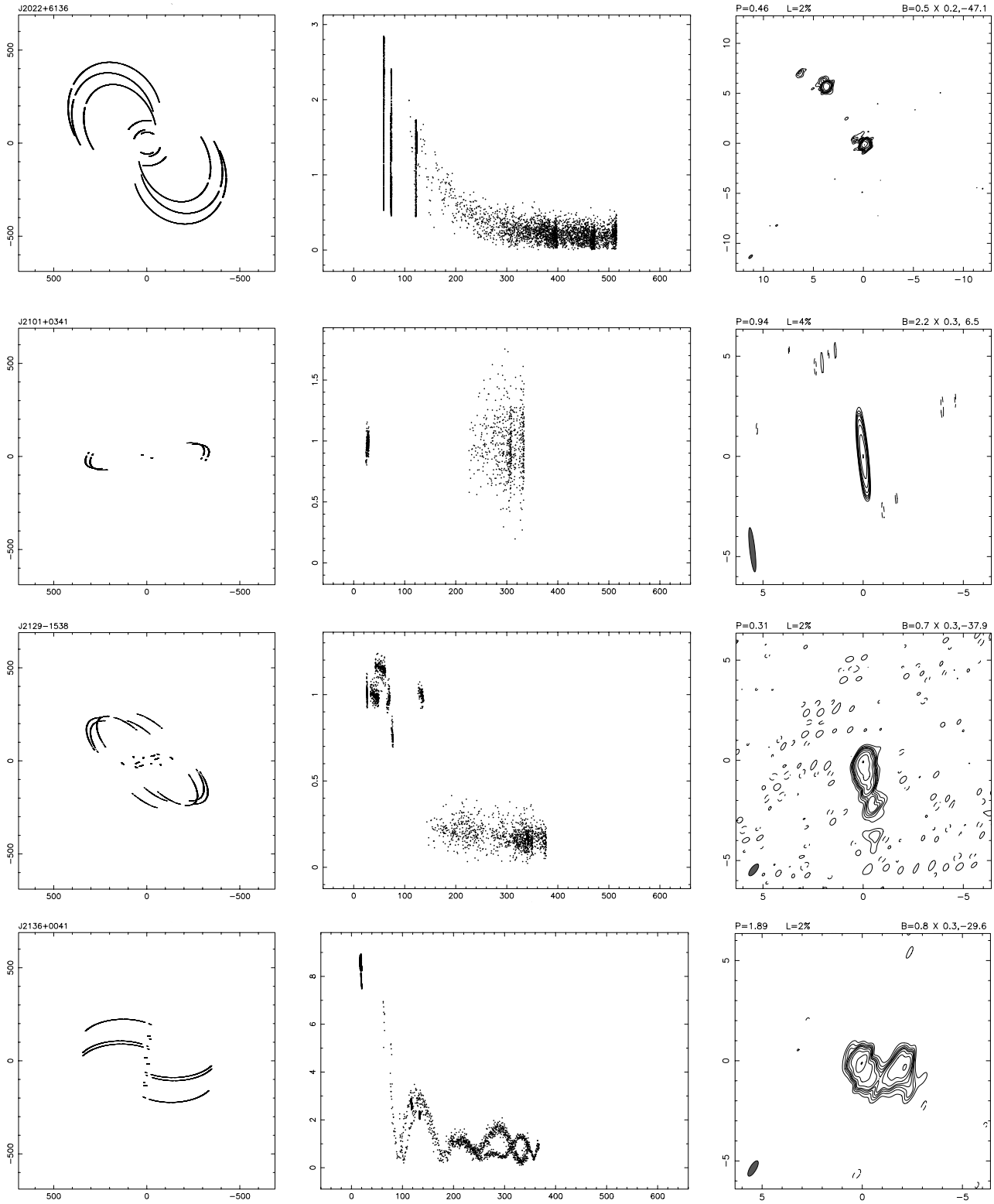

FIG. 2.—*Continued*

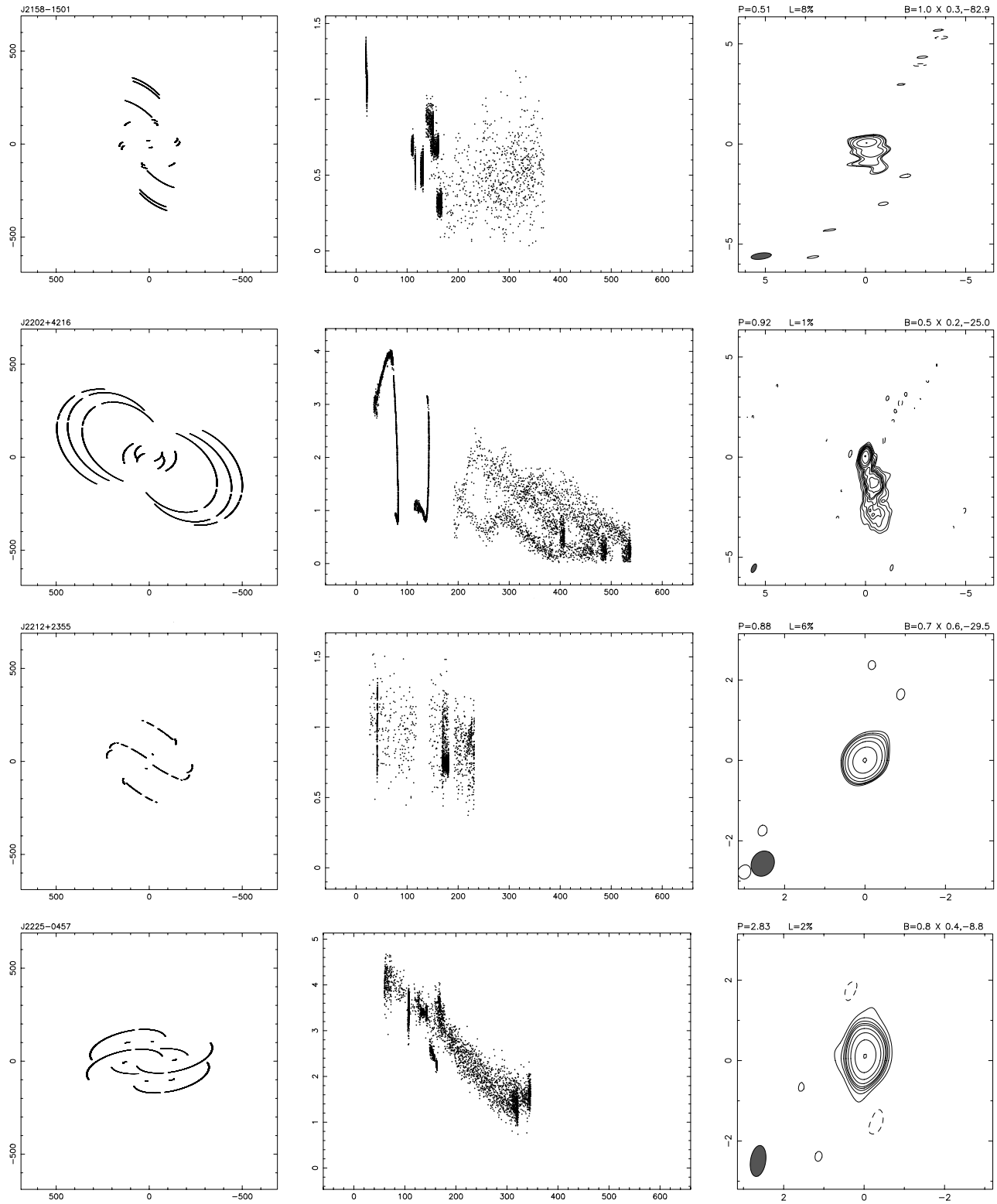

FIG. 2.—*Continued*

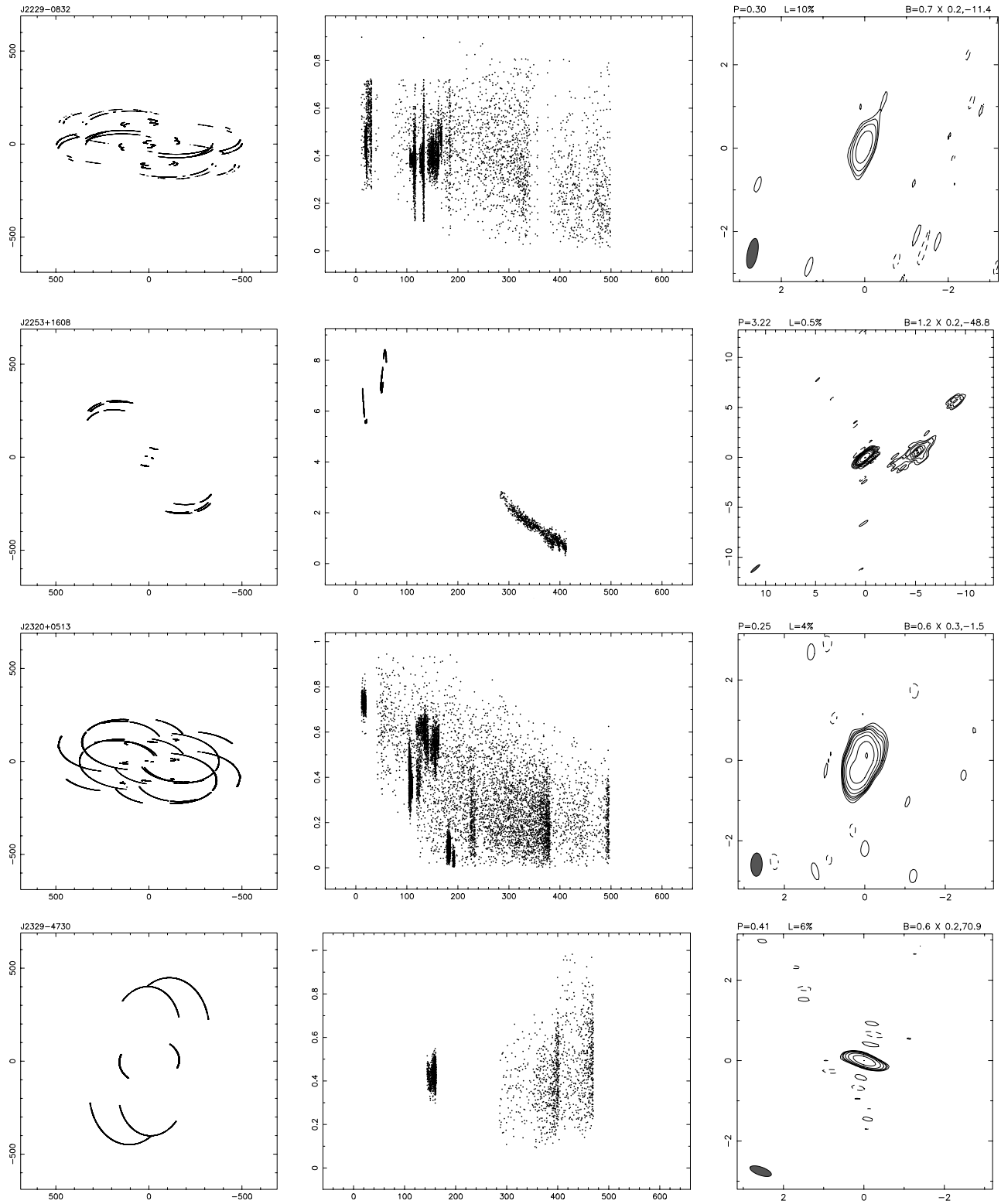

FIG. 2.—*Continued*

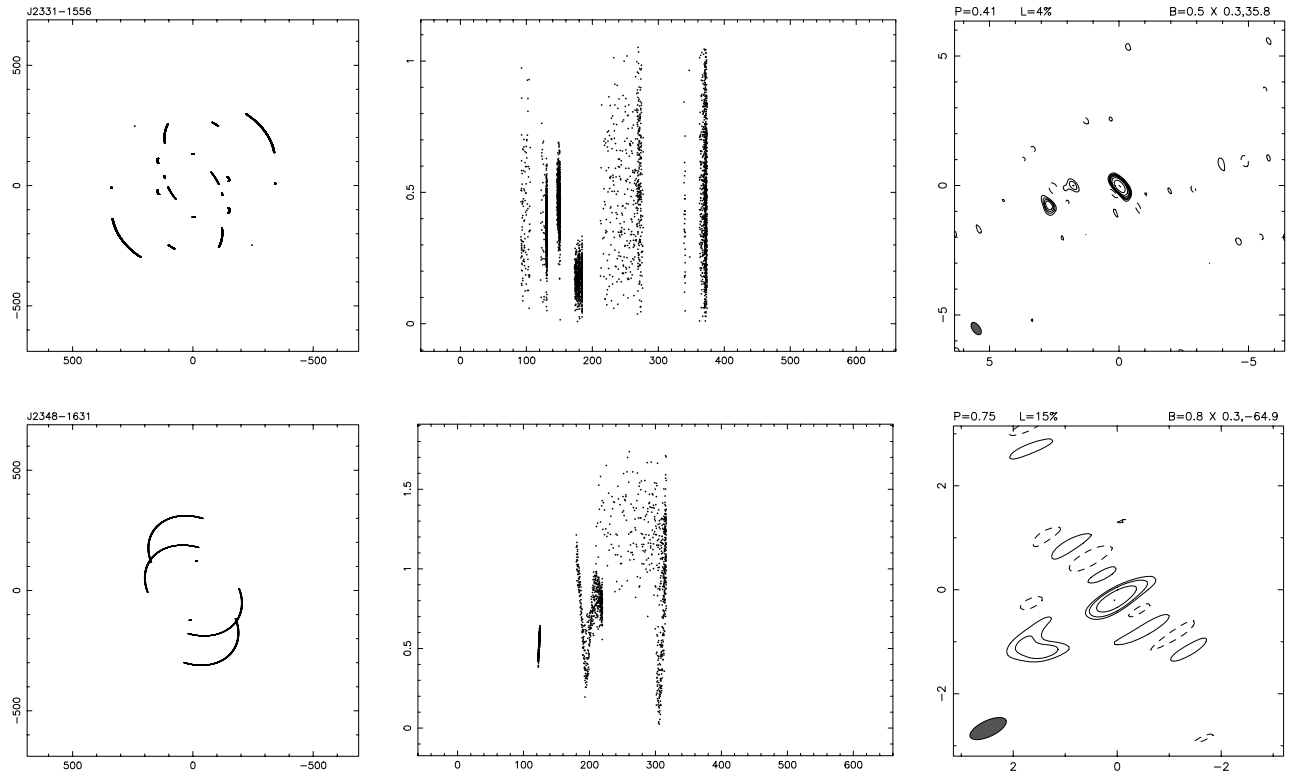

FIG. 2.—*Continued*

In order to ensure that the lower sensitivity *HALCA* data were not largely ignored during the model-fitting they were upweighted to give them a weight comparable to the ground baseline data (Lovell et al. 2004). The parameters for all the components are listed in Table 2. The flux density errors due to the fitting are typically 0.03 Jy, or 10% of the component flux density, whichever is greater, giving a total error in the flux density parameters (including the error in the overall visibility amplitude scaling) of approximately 0.03 Jy, or 25% of the component flux density.

The lower error bound for the diameter of a component is given by

$$D_{-} = \sqrt{[D^2 + B^2][1 - (1/S)]^2 - B^2}, \qquad (1)$$

where D is the FWHM diameter of the component, B is HPBW in the direction of D, and S is the signal-to-noise ratio associated with the component (Fomalont et al. 2000a). When the argument of the square root is negative, then the lower error bound on the diameter is zero. In this case, the component was assumed to be consistent with a zero diameter component (either a δ-function or zero axial ratio elliptical Gaussian), and the diameter was set to zero.

For each source the brightness temperature of the core was determined using the model-fit components. The brightness temperature of a component in the observer's frame is given by

$$T_b = \frac{S\lambda^2}{2k_{\rm B}\Omega}, \qquad (2)$$

where S is the component flux density at wavelength λ, $k_{\rm B}$ is Boltzmann's constant, and $\Omega \approx 1.13(B_{\rm maj})(B_{\rm min})$ is the solid angle subtended by the component (which we have expressed in terms of the full width at half-maximum of the component major and minor axes). To convert to brightness temperature in the source frame, equation (2) is multiplied by $(1 + z)$, where z is the source redshift.

The error in the $B_{\rm maj}$ and $B_{\rm min}$ component parameters, when the core is resolved, is approximately 10%, giving an error in the solid angle subtended by the components of approximately 15%. When combined with the approximately 25% error in the component flux densities, this implies an error in the brightness temperature for resolved components of about 30%.

The determination of the core component was based upon the morphology of the source, VLBI images of the source at other frequencies, and/or identifications from external references. With the exception of J1723−6500, a GPS source whose core was probably not detected, the core brightness temperatures are listed in Table 2. However, considerable caution should be exercised when the core component overlaps one or more other components. Overlapping components are denoted by an asterisk (*) or dagger (†) in the flux density column in Table 2. We have defined "overlapping" to mean that a component's position (in the case of a δ-function) or FWHM is located within or overlaps the FWHM of another component. In addition, caution should be exercised in any interpretation of the major axis position angle of the core component. Lister et al. (2001) has found that for unequal (u, v) plane coverage, the major axis position angle of the core component is strongly correlated with that of the beam and is therefore unlikely to reflect an intrinsic property of the source.

A lower bound on the brightness temperature of unresolved cores was determined using the Difwrap software package (Lovell 2000). Difwrap is a Perl language graphical user interface for the Difmap software package. Using Difwrap, the (component flux density, component size) parameter space was searched to find the combination of parameters that had

TABLE 2

SOURCE COMPONENT PARAMETERS

Source (1)	S (Jy) (2)	Rad (mas) (3)	Phi (deg) (4)	B_{maj} (mas) (5)	B_{min} (mas) (6)	P.A. (deg) (7)	$T_b \times 10^{12}$ (K) (8)
J0006−0623	1.29*	0.0	...	0.5	0.0	17	>0.48
	1.50*	0.6	−67	4.4	0.5	−79	
J0019+7327	0.06*	0.2	94	0.0	0.0	...	>0.17
	0.47*	0.1	152	1.1	0.6	−61	
J0042+2320	0.29	0.0	...	0.2	0.2	...	0.29
J0106−4034	2.93	0.0	...	0.3	0.0	−5	>3.79
J0115−0127	0.36	0.1	−38	0.6	0.1	−37	0.25
	0.55	1.0	114	1.4	0.1	−53	
J0121+1149	1.92	0.0	...	1.5	0.3	−1	0.27
J0126+2559	0.60	0.2	165	0.0	0.0	...	>0.04
	0.16	1.9	−175	0.0	0.0	...	
J0136+4751	1.82	0.0	...	0.2	0.1	−14	4.27
	0.36	0.6	−33	1.2	0.3	−3	
J0210−5101	0.72	0.1	−100	0.4	0.2	51	0.46
	1.83	1.9	−111	0.8	0.7	−24	
J0217+7349	0.47*	0.2	50	0.2	0.2	...	0.50
	2.42*	0.0	...	0.8	0.3	−63	
J0251+4315	0.57	0.0	...	0.4	0.4	...	0.20
	0.27	1.7	143	0.3	0.3	...	
	0.07	0.9	156	0.0	0.0	...	
J0319+4130	1.01	1.7	12	0.8	0.8	...	0.08
	1.59	0.3	−1	1.2	0.8	−19	
	1.00	1.0	−33	2.5	0.5	3	
	0.94	10.5	10	1.7	1.7	...	
	0.68	7.0	−164	1.1	1.1	...	
	0.30	2.4	177	1.0	1.0	...	
J0334−4008	0.49	0.0	...	0.0	0.0	...	>0.60
J0348−2749	0.84	0.0	...	0.3	0.1	−69	1.13
	0.31	1.2	136	1.2	1.2	...	
J0403−3605	1.16	0.0	...	0.5	0.2	21	0.79
	0.20	2.6	37	0.7	0.4	10	
J0405−1308	0.76	0.1	47	0.2	0.2	...	0.98
J0423−0120	2.68	0.0	...	0.3	0.3	...	1.90
J0440−4333	0.75*	0.0	...	0.2	0.2	...	1.66
	0.46*	0.3	105	0.6	0.6	...	
J0453−2807	0.38	0.1	156	0.2	0.1	−18	1.08
	0.40	0.3	12	0.8	0.3	−31	
J0457−2324	4.21	0.0	...	0.4	0.4	...	1.40
J0501−0159	0.66	0.1	−12	1.0	0.2	−16	0.16
	0.04	1.0	−28	0.0	0.0	...	
J0538−4405	0.57	0.0	...	0.2	0.2	...	0.82
	0.42	0.8	72	0.5	0.5	...	
J0539−2839	1.63	0.0	...	0.2	0.1	84	3.47
J0542+4951	0.14	0.0	...	0.0	0.0	...	>0.07
	0.36	1.0	−126	1.7	1.3	3	
J0555+3948	4.72	0.0	...	0.4	0.4	...	1.63
	2.57	0.7	−53	0.6	0.6	...	
J0607−0834	0.78	0.0	...	0.3	0.1	−51	1.25
	0.41	1.1	126	0.6	0.6	...	
	0.16	2.0	103	0.9	0.9	...	
J0609−1542	2.13	0.0	...	0.0	0.0	...	>3.79
	0.65	0.8	58	1.0	0.2	−18	
J0635−7516	3.50*	0.1	−10	0.7	0.4	−76	0.71
	5.68	1.7	−87	1.1	1.1	...	
	1.69*	0.3	−106	0.9	0.1	−80	
J0714+3534	0.76	0.0	...	0.7	0.5	−65	0.10
	0.19	5.8	157	0.7	0.2	−46	
	0.13	1.5	160	0.8	0.8	...	
J0738+1742	0.58	0.0	...	0.2	0.2	...	0.77
	0.11	1.0	70	0.7	0.7	...	
J0741+3112	3.52	0.1	29	0.4	0.4	...	1.05
	1.27	2.6	0	0.4	0.4	...	

TABLE 2—*Continued*

Source (1)	S (Jy) (2)	Rad (mas) (3)	Phi (deg) (4)	B_{maj} (mas) (5)	B_{min} (mas) (6)	P.A. (deg) (7)	$T_b \times 10^{12}$ (K) (8)
J0748+2400	0.52	0.0	...	0.6	0.0	−63	>0.19
	0.11	3.4	−60	0.3	0.3	...	
J0811+0146	0.67	0.1	141	0.6	0.2	−30	0.40
	0.13	0.7	163	0.0	0.0	...	
J0818+4222	0.58	0.0	...	0.2	0.1	−74	1.16
	0.37	1.1	86	0.8	0.8	...	
J0824+5552	0.75	0.0	...	0.4	0.2	−74	0.47
J0836−2016	1.64	0.0	...	1.0	0.8	30	0.11
J0841+7053	0.27*	0.1	11	0.0	0.0	...	>0.12
	0.66†	2.1	−142	2.5	0.5	25	
	0.64*	0.1	−133	0.7	0.2	34	
	0.11†	2.6	−140	0.0	0.0	...	
J0854+2006	0.40	0.2	33	0.0	0.0	...	>0.07
	1.42	0.1	−61	0.3	0.2	57	
	0.30	0.9	−91	0.4	0.2	60	
J0903+4651	0.39*	0.1	172	0.9	0.1	−25	0.25
	0.35*	0.5	125	1.2	1.2	...	
	0.27	1.5	1	2.0	1.0	−28	
J0909+0121	0.97	0.0	...	0.4	0.2	−23	0.58
	0.08	1.0	29	0.5	0.5	...	
J0920+4441	0.33	0.1	−26	0.0	0.0	...	>0.07
	0.58	0.9	179	0.8	0.6	28	
	0.28	0.6	7	0.5	0.3	−70	
J0927+3902	9.67	0.2	136	0.5	0.5	...	1.96
	0.95	0.6	97	0.0	0.0	...	
J1037−2934	1.11	0.1	−160	0.5	0.3	−49	0.33
	0.22	0.7	125	0.6	0.6	...	
J1048+7143	1.84	0.0	...	0.3	0.1	−28	2.23
J1058+0133	1.02	0.0	...	0.2	0.2	...	2.26
	0.60	1.8	−47	0.7	0.4	−72	
	0.23	6.0	−49	2.7	1.2	−19	
J1107−4449	2.13	0.3	151	0.7	0.4	74	0.41
J1118+1234	0.51	0.0	...	0.6	0.0	10	>0.30
J1146−2447	0.44	0.1	−124	0.5	0.3	32	0.15
	0.23	3.8	175	1.4	0.6	−21	
J1147−0724	0.74	0.0	...	0.5	0.3	21	0.27
J1147−3812	2.08	0.0	...	0.2	0.2	...	1.81
J1215−1731	1.05	0.0	...	0.2	0.2	...	2.11
	0.09	0.7	108	0.0	0.0	...	
J1229+0203	3.07	0.6	−146	0.6	0.6	...	0.50
	5.26	1.9	−116	4.6	0.0	63	
	1.64	6.3	−110	0.6	0.6	...	
	0.13	7.9	−115	0.0	0.0	...	
J1230+1223	0.18	0.7	93	0.0	0.0	...	>0.23
	1.61*	2.5	−76	3.2	3.2	...	
	0.60	0.4	18	0.8	0.4	−38	
	0.42*	0.9	−80	1.5	0.0	50	
J1246−2547	0.68	0.1	37	0.2	0.2	...	0.71
	0.11	0.6	142	0.4	0.4	...	
J1256−0547	7.93	0.2	−145	0.7	0.3	40	2.02
	5.75	3.2	−113	1.3	0.3	11	
J1310+3220	1.39	0.0	...	0.2	0.2	...	1.25
	1.07	1.1	−58	0.4	0.4	...	
J1337−1257	3.72	0.0	...	0.5	0.2	13	1.73
	0.33	0.7	−128	0.0	0.0	...	
J1357−1744	0.32*	0.0	...	0.3	0.3	...	0.26
	0.77*	0.1	−108	1.4	1.0	39	
J1407+2827	0.06*	0.2	123	0.0	0.0	...	>0.07
	1.89*	0.0	...	1.5	0.7	−19	
J1430+1043	0.79	0.1	−153	1.1	0.2	17	0.22
J1507−1652	0.93	0.2	−159	0.5	0.1	26	0.97
J1510−0543	0.55	0.0	...	0.2	0.2	...	0.53
J1512−0905	1.62	0.1	7	0.4	0.1	−18	1.96
	0.28	1.7	−39	0.9	0.9	...	

TABLE 2—*Continued*

Source (1)	S (Jy) (2)	Rad (mas) (3)	Phi (deg) (4)	$B_{\rm maj}$ (mas) (5)	$B_{\rm min}$ (mas) (6)	P.A. (deg) (7)	$T_b \times 10^{12}$ (K) (8)
J1517−2422	1.04	0.1	170	0.9	0.1	−5	1.11
	0.15	0.9	168	0.0	0.0	...	
	0.11	1.5	171	0.0	0.0	...	
J1549+0237	1.59*	0.0	...	0.8	0.1	0	1.56
	0.45*	0.4	157	1.0	0.0	−46	
J1613+3412	1.05	0.0	...	0.2	0.0	0	>0.95
J1617−7717	0.24*	0.2	102	0.0	0.0	...	>0.04
	2.51*	0.2	−77	1.1	0.5	−70	
J1626−2951	0.59*	0.1	86	0.4	0.3	29	0.27
	1.12*	0.2	−75	0.7	0.4	−72	
J1635+3808	0.42	0.7	107	0.0	0.0	...	>0.30
	0.96	1.1	−92	1.0	0.8	64	
	0.69	0.2	134	0.6	0.3	−53	
J1638+5720	0.17	1.0	22	0.0	0.0	...	>0.04
	0.29	0.0	...	0.0	0.0	...	
J1640+3946	1.03	0.0	...	0.4	0.3	−47	0.49
J1642+3948	1.77	0.0	...	0.4	0.2	23	0.99
	2.64	1.4	−100	1.4	0.0	−81	
	2.25	0.7	−103	0.6	0.3	−19	
J1642+6856	0.14	0.4	11	0.0	0.0	...	>0.04
	0.34	0.2	32	0.0	0.0	...	
	0.23	1.0	179	0.7	0.4	−44	
J1653+3945	0.48	0.0	...	0.2	0.2	...	0.58
	0.21	2.2	147	1.3	1.3	...	
J1658+0515	0.30	0.6	−104	0.3	0.3	...	0.19
	0.45	0.0	...	0.2	0.2	...	
J1658+0741	0.33	0.5	162	0.2	0.2	...	0.32
	0.96	0.1	−11	0.3	0.3	...	
	0.21	7.6	−44	0.7	0.7	...	
J1723−6500	1.59	6.6	134	1.4	1.0	9	
	1.39	0.0	...	1.1	0.7	−12	
J1733−1304	5.14	0.0	...	0.5	0.3	20	1.72
J1740+5211	2.25	0.0	...	0.4	0.3	−28	1.21
J1751+0939	1.56	0.1	−22	0.1	0.1	...	6.67
	0.50	0.6	45	2.1	0.7	−3	
J1800+7828	1.42	0.0	...	0.2	0.2	...	2.68
	0.53	1.4	−97	0.8	0.5	61	
	0.34	0.5	−89	0.4	0.4	...	
J1806+6949	0.58	0.0	...	0.4	0.1	71	0.76
	0.26	0.7	−102	0.9	0.2	−78	
J1824+5651	0.91	0.1	−168	0.6	0.1	17	0.99
	0.27	1.0	−163	0.9	0.2	46	
	0.11	1.8	−157	0.4	0.4	...	
J1902+3159	0.64	0.1	42	0.4	0.2	−11	0.41
	0.23	15.5	119	1.2	1.2	...	
	0.22	0.9	127	0.7	0.2	−36	
J1924−2914	1.97	0.2	158	0.0	0.0	...	>0.76
	6.42	1.1	3	0.5	0.5	...	
J1939−1525	0.64	0.0	...	0.1	0.1	...	1.43
J2000−1748	2.00	0.1	138	0.3	0.2	−47	2.53
J2005+7752	1.27	0.0	...	0.6	0.1	−84	0.77
	0.17	1.2	−99	0.3	0.3	...	
J2022+6136	0.13	1.0	62	0.8	0.2	−29	0.04
	1.19	6.8	33	0.9	0.7	58	
	0.94*	0.3	−131	0.6	0.4	−57	
	0.69*	0.1	−91	0.6	0.3	−16	
	0.14	9.5	41	0.9	0.3	−36	
J2101+0341	0.67	0.0	...	0.0	0.0	...	>0.60
J2129−1538	0.16*	0.0	...	0.0	0.0	...	>0.20
	1.00*	0.8	−168	2.1	0.3	10	
J2136+0041	2.81	0.1	170	0.5	0.1	30	2.46
	3.16	2.2	−91	1.1	0.0	12	
	2.00	1.6	−113	0.9	0.9	...	
	0.71	0.8	−159	0.5	0.5	...	

TABLE 2—*Continued*

Source (1)	S (Jy) (2)	Rad (mas) (3)	Phi (deg) (4)	B_{maj} (mas) (5)	B_{min} (mas) (6)	P.A. (deg) (7)	$T_b \times 10^{12}$ (K) (8)
J2158−1501	0.46	0.1	−22	0.0	0.0	...	>0.24
	0.74	0.5	−150	1.0	0.6	2	
J2202+4216	0.92	0.1	18	0.1	0.1	...	3.09
	1.71	1.4	−163	0.6	0.6	...	
	1.02	0.2	−162	0.2	0.2	...	
	0.76	2.8	−169	0.8	0.8	...	
J2212+2355	1.00	0.0	...	0.3	0.1	−57	1.43
J2225−0457	3.88	0.1	−12	0.4	0.2	49	2.31
J2229−0832	0.43	0.1	19	0.2	0.2	...	0.38
J2253+1608	7.73	0.0	...	0.4	0.4	...	2.29
	1.44	5.2	−83	0.7	0.7	...	
	0.90	7.0	−72	1.4	1.4	...	
J2320+0513	0.21	0.5	147	0.3	0.2	42	0.20
	0.54	0.1	−16	0.6	0.3	−12	
J2329−4730	0.41	0.0	...	0.0	0.0	...	>0.30
J2331−1556	0.45	0.0	...	0.0	0.0	...	>0.16
	0.27	2.8	109	1.9	0.0	−35	
J2348−1631	0.75	0.2	171	0.0	0.0	...	>0.19
	0.71	1.9	124	0.6	0.6	...	

NOTES.—Col. (2): The integrated flux density of the component; asterisk (*) and dagger (†) denote overlapping components (see text). Col. (3): The radial distance of the component center from the center of the map. Col. (4): The position angle of the center of the component, measured counterclockwise from an imaginary vertical line from the map center toward the north. Col. (5): The FWHM of the major axis of the component. Col. (6): The FWHM of the minor axis of the component. Col. (7): The position angle of the major axis of the component, measured from the north toward the east. Col. (8): The brightness temperature of the component. Table 2 is also available in machine-readable form in the electronic edition of the *Astrophysical Journal Supplement*.

the lowest brightness temperature, but still had an adequate fit to the data [based upon plots of visibility amplitude vs. (u, v) radius]. For a fit to be adequate the model still had to retain the essential structure of the amplitude versus (u, v) plot. However, small deviations between the model and the visibility data, of the order of 20% or so, were allowed. For each point in the parameter space the best fit in position was determined using the Difmap `modelfit` command. All other components were kept fixed. Although subjective, visually comparing the model fits to the data is thought to be a conservative estimate of the parameter errors (Tzioumis et al. 1989).

The error estimate for the brightness temperature lower limits will be greater than the error in the brightness temperature of resolved sources, owing to the additional subjectivity in assessing what comprises an "adequate fit." An error of ±50% is probably reasonable.

Histograms depicting the frequency of occurrence of the brightness temperature in both the source and observer's frame are shown in Figure 3. Most cores have $T_b > 10^{11}$ K, with approximately 54% of the sources having a brightness temperature (or brightness temperature lower limit) in excess of 10^{12} K in the source frame, and approximately 38% of the sources having a brightness temperature (or brightness temperature lower limit) greater than 10^{12} K in the observer's frame.

The source with the highest core brightness temperature in the source frame is J0539−2839, with $T_b = 1.2 \times 10^{13}$ K.

We can compare our brightness temperature distribution with distributions obtained by other groups using space VLBI data. The first brightness temperature determinations using space VLBI were calculated from observations using a 4.9 m diameter orbiting antenna, which was part of the Tracking and Data Relay Satellite System (TDRSS; Levy et al. 1989). At 2.3 GHz, Linfield et al. (1989) found that 10 out of 14 sources (71%) had source frame brightness temperatures in excess of 10^{12} K, while at 15 GHz six out of nine sources (66%) had source frame brightness temperatures in excess of 10^{12} K (Linfield et al. 1990). Considering the relatively small number of sources in these samples, this is in reasonable agreement with our results. In addition, using general observing time VSOP data, brightness temperatures have been calculated for a selection of sources from the Pearson-Readhead source sample (Pearson & Readhead 1988). Lister et al. (2001) has calculated the observer-frame brightness temperature for a selection of 27 of these sources, while (Tingay et al. 2001) has calculated the comoving frame brightness temperature for 31 sources from this sample. Approximately 26% of the source frame brightness temperatures were in excess of 10^{12} K, while approximately 19% of the sources had comoving frame brightness temperatures in excess of 10^{12} K. While this latter result is considerably smaller than our result, Tingay et al. (2001) normalized all their brightness temperatures to brightness temperatures at a fixed frequency in the comoving frame, which reduced their brightness temperatures by a factor of $(1+z)^{1/2}$ when compared to our results. In addition, Tingay et al. (2001) calculated source brightness temperatures assuming an optically thick core, which reduced their brightness temperatures by an additional factor of 0.56 with respect to our results. Multiplying the Tingay et al. (2001) brightness temperatures by $(1+z)^{1/2}/0.56$ results in about 48% of their source frame brightness temperatures exceeding 10^{12} K, approximately the same percentage as was seen in this paper.

The distribution of the angular size of the cores is plotted in Figure 4. The median angular size subtended by the resolved cores is about 0.075 mas^2, corresponding to an angular diameter (FWHM) of approximately 0.26 mas. Of course, the former

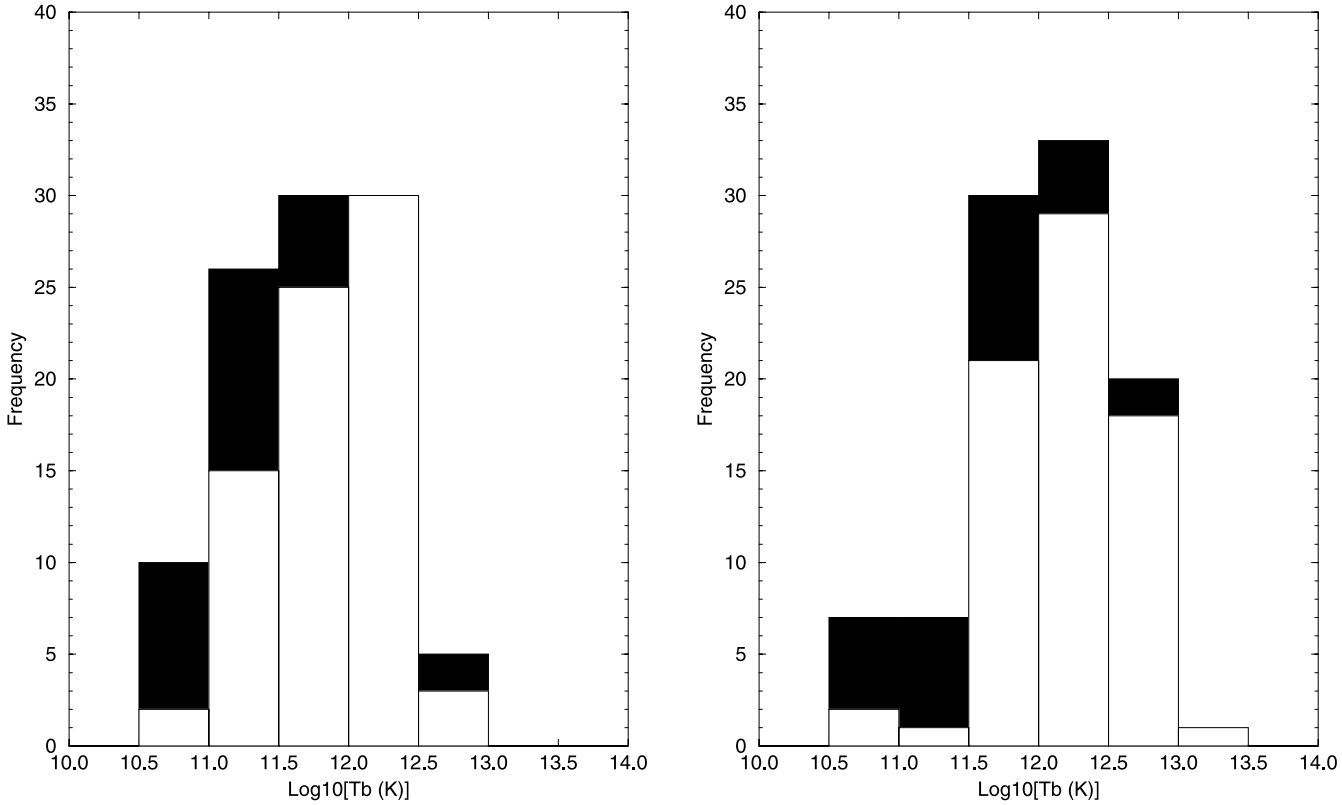

FIG. 3.—Histogram of core brightness temperatures: The core brightness temperature for the 101 Survey sources with identified cores (i.e., excluding J1723−6500) has been binned, with $\log_{10}(T_b)$ on the abscissa, and the frequency per bin as the ordinate. The open histogram has been used for those sources with resolved cores. The shaded portion of the histogram represents brightness temperature lower limits for unresolved cores. On the left is the brightness temperature distribution in the observer's frame, while the histogram on the right represents the brightness temperature distribution in the source frame. The source frame histogram only depicts brightness temperatures from 98 of the sources, since the redshift for three of the 101 sources was unknown.

value only represents a median of core sizes for which the interferometer was sensitive to. Any cores with extremely small angular size (FWHM $\approx$ 0.1 mas or less, for instance) are unresolved and have not been incorporated into the calculation of the median. In addition, any large-scale structure around the core may not have been detected [depending upon the (u, v) plane coverage on shortest baselines], which may have rendered the core size estimation for several of the sources artificially low. Hence, any physical interpretation of the median core size should be treated with caution.

3.3. *Comments on Individual Sources*

When applicable, short notes on the sources are given. In addition, a general comparison is made with VLBI images from other sources, primarily the VLBApls (Fomalont et al. 2000a), US Naval Observatory Database (USNO; Fey et al. 1996; Fey & Charlot 1997, 2000), a space VLBI Survey of Pearson-Readhead sources (VSOPPR; Lister et al. 2001), the VLBA 2 cm Survey (VLBA2cm1; Kellermann et al. 1998; Zensus et al. 2002, and VLBA2cm2; L. I. Gurvits, K. I. Kellermann, E. B. Fomalont, & H. Y. Zhang 2004, in preparation), and results from VSOP observations of southern sources (VSOPsth; Tingay et al. 2002). Any significant differences are noted. When the core is unresolved, a limit on the area subtended by the core is given.

J0006−0623.—The data quality for this source is relatively poor. The extended emission is only fitted to a single component because of a paucity of baselines less than 100 Mλ in length. The area subtended by the core is less than 0.2 mas^2.

J0019+7327.—An image with the full GOT data set is given in VSOPPR. The VLBA2cm1 images show significant evolution of this source between 1994 and 2000. The size and orientation of the VSOP image is consistent with the VLBA2cm1 image in 1998 March. The area subtended by the core component is less than 0.03 mas^2.

J0042+2320.—The VSOP image contains much less flux density than that in the VLBApls and USNO. It may be variable. The USNO 8.6 GHz image shows an extension 3 mas to the north-northeast, and an elongation of the core to the south. The VLBA2cm2 image has an additional component to the south. The VLBApls image, however, shows an extension to the east.

J0106−4034.—The area subtended by the core component is less than 0.05 mas^2.

J0115−0127.—The central region has been resolved into two separate components. We have assumed the more northern component is the core. The P.A. of the jet in the Survey image is slightly more northerly than the P.A. of the jet seen in lower resolution images.

J0121+1149.—In 5 GHz observations by Gabuzda et al. (1999) the core was unresolved, although in the VLBA2cm1 and USNO images the core has an asymmetry toward the north. In addition, there is extended emission north of the core in the VLBApls and USNO 2 GHz images.

J0126+2559.—The data quality is poor, but the VSOP image is consistent with those of the VLBApls and USNO images. The area subtended by the core component is less than 1 mas^2.

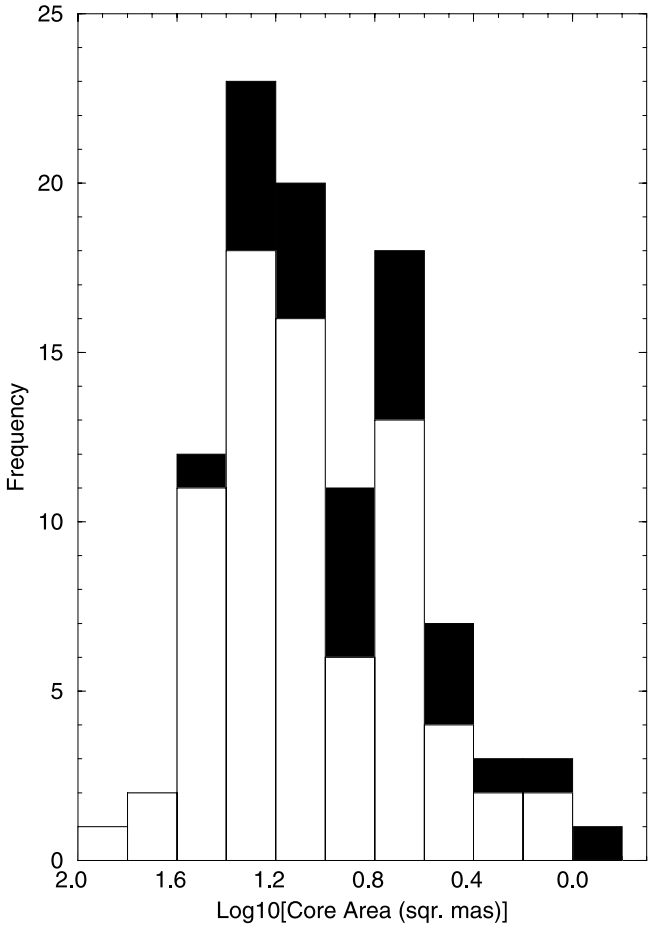

FIG. 4.—Histogram of core angular sizes: The core area for the 101 Survey sources with identified cores (i.e., excluding J1723−6500) has been binned, with $\log_{10}$(core area) on the abscissa, and the frequency per bin as the ordinate. The open histogram has been used for those sources with resolved cores. The shaded portion of the histogram represents upper limits on the core size for unresolved cores.

J0136+4751.—Most of the emission is in a small, central component. The emission to the north is strong at low frequencies, and the component to the northwest is stronger at high frequencies. The VLBA2cm1 observations show this northwest component decreasing in flux density with time.

J0210−5101.—An image with the full GOT data set is given in VSOPsth. We have assumed the more compact northeastern component is the core.

J0217+7349.—The central region is resolved into two closely spaced components. We have assumed the core is the more compact of the components. An image made using all the GOT data can be found in VSOPPR.

J0251+4315.—The USNO, VLBApls, and VLBA2cm2 show a large component around 15 mas to the southeast. We have assumed that the core is the most northwesterly component of the strong, central emission region.

J0319+4130.—(3C 84) Images using GOT data can be found in VSOPPR and Asada et al. (2000). The six-component model fit does not account for some of the large-scale structure. Following Vermeulen et al. (1994) we have identified the core as the most northeasterly component of the strong, central emission region.

J0334−4008.—The redshift for this source is quoted from Hewitt & Burbidge (1987), although there appears to be little support for this value. Drinkwater et al. (1997) were unable to find a redshift for this source. The area subtended by the core component is less than 0.07 mas^2.

J0403−3605.—The core is extended to the northeast, in the direction of faint extended emission seen by the VLBApls, USNO, and VLBA2cm2 images.

J0405−1308.—Extended emission to the south, as seen in the VLBApls and VLBA2cm2 images, is not seen in the VSOP image, possibly because of the lack of VSOP data on short spacings.

J0423−0120.—In the USNO and VLBA2cm1 images there is additional emission south of the core component.

J0440−4333.—An image made from the entire GOT data set is found in VSOPsth. We have separated the emission into two components, one of which is unresolved. The one-component fit used in VSOPsth contains both components reported here.

J0453−2807.—The inner jet points in the direction of the larger scale structure seen in the VLBApls.

J0457−2324.—VLBApls image has a faint component extending off the core to the west.

J0501−0149.—We have assumed the core is the stronger component to the southeast.

J0538−4405.—An image made from all the GOT data is found in VSOPsth.

J0539−2839.—The core is resolved and is elongated toward the extended structure seen in the VLBApls. ATCA light curves (Tingay et al. 2003) indicate a dramatic increase in flux over the 40 months between the VLBApls and the VSOP observation. The VLBA2cm2 image has a small additional component to the east.

J0542+4951.—(3C 147) The source is composed of a core component with diffuse emission to the west. See also the VSOP image from Slysh et al. (2001). The area subtended by the core is less than 0.10 mas^2.

J0555+3948.—The jet to the west, seen in the VLBA2cm1 and VLBA2cm2 images, is clearly seen in the VSOP image. The data were very well modeled by two circular Gaussians, one each for the core and jet components.

J0609−1542.—The core, as seen in the VLBApls image, is now clearly resolved out into two distinct components. Emission in the core region, as seen in the VSOP image as well as higher frequency USNO ground images, is mostly in an easterly direction. Lower resolution images show the jet taking a more northeasterly tack farther from the core. The area subtended by the core is less than 0.05 mas^2.

J0635−7516.—An image made from all the GOT data is found in VSOPsth. The core is complex and extended. We have used the easternmost component in our determination of core brightness temperature.

J0741+3112.—This is a GPS source (Stanghellini et al. 1997). The VLBApls image is resolved out into two components in our Survey image. However, the P.A. of the eastern extension of the southern component is not consistent with P.A. of a similar extension in the VLBApls, USNO, and VLBA2cm1 images, probably due to insufficient short spacing data. The southern component is the most compact, hence, this may be the core. The redshift and optical ID is taken from Hewitt & Burbidge (1993).

J0748+2400.—The area subtended by the core is less than 0.2 mas^2.

J0811+0146.—USNO images indicate a possible bent jet morphology, with the jet direction toward the south near the core, then bending toward the west. The VSOP image of the core region is consistent with this morphology.

J0818+4222.—An image made from all the GOT data is found in VSOPPR. The redshift was obtained from Lawrence et al. (1996).

J0824+5552.—Both 2 and 8 GHz USNO images show a jet aligned in a northeasterly direction.

J0841+7053.—An image made from the entire GOT data set can be found in VSOPPR. This is a complex source with an faint unresolved core. We have identified the core to be the most northerly component. The redshift was obtained from Jackson et al. (2002). The area subtended by the core is less than 0.1 mas^2.

J0854+2006.—(OJ 287) A VSOP GOT image is given in Gabuzda & Gómez (2001), who identify the core as the unresolved component to the northeast of the strongest component. The area subtended by the core is less than 0.3 mas^2.

J0903+4651.—The jet to the north seen in other VLBI images is not seen in our VSOP image, probably due to the poor (u, v) plane coverage. The complex core region has been resolved into two closely spaced components.

J0909+0121.—There is some emission seen toward the larger scale structure seen in the VLBApls, USNO, and VLBA2cm1 images.

J0920+4441.—This is a complex source. We have assumed the core to be the strong, compact, central component. There is extended emission on both sides of this core. The area subtended by the core is less than 0.3 mas^2.

J0927+3902.—(4C 39.25) An image made from VSOP GOT data can be found in VSOPPR. The main component is slightly asymmetric, with a small component that is east of the main body of the source. Higher frequency USNO images suggest that the core is the more central, stronger component.

J1058+0133.—See VLBApls, USNO, VLBA2cm1, and VLBA2cm2 for more detailed images of the extended emission to the northwest. Based upon the USNO higher frequency images, the core appears to be the easternmost component.

J1107−4449.—The image from the complete GOT data set is given in VSOPsth.

J1118+1234.—See VLBA2cm2 for a more detailed image. The area subtended by the core is less than 0.1 mas^2.

J1146−2447.—This is a GPS source (Stanghellini et al. 1997). The secondary component to the south coincides with the extended emission seen in the VLBApls and 8 GHz USNO images.

J1147−0724.—The core region extends westward toward the extended emission seen in the VLBApls, USNO, and VLBA2cm1 images.

J1147−3812.—Faint emission to the east is also seen in some of the 8 GHz USNO images.

J1215−1731.—Stickel & Kühr (1996) were able to get an optical ID for this source, despite the close proximity of the star gamma Corvus.

J1229+0203.—(3C 273) A VSOP image made from GOT data can be found in Lobanov & Zensus (2001). The four-component model-fit does not include the large-scale structure.

J1230+1223.—(3C 274, M87) A VSOP image made from GOT data can be found in Junor et al. (2000). The four-component model fit only accounts for the small-scale structure. The faint core is unresolved subtending an area of less than 0.05 mas^2.

J1246−2547.—The extension from the core is in the same direction as the extended emission seen in the VLBApls and VLBA2cm2 images.

J1256−0547.—(3C 279) For the GOT images of this source see Piner et al. (2000). The core has been identified as the stronger, easternmost component (Piner et al. 2000).

J1310+3220.—Based upon 8, 24, and 43 GHz USNO images we have assumed the core to be the more easterly component.

J1337−1257.—The faint component to the west of the main component is seen in VLBA2cm1 images after 1999, so it is probably a new component.

J1357−1744.—A VLBA image at 5 GHz (Frey et al. 1997) shows a weak, 10 mas scale bent jet extending toward the southeast and east.

J1407+2827.—(OQ 208) The area subtended by the faint core is less than 0.04 mas^2.

J1507−1652.—VLBA2cm1 images, as well as the 8 and 15 GHz USNO images, show extended structure to the south and southeast. This extended structure is not as apparent in our image owing to poor sampling of the short (u, v) spacings.

J1510−0543.—The extended emission to the east seen in the VLBApls, VLBA2cm1, and VLBA2cm2 images is not seen in our image, probably because of the paucity of data on shorter baselines.

J1512−0905.—The redshift for this source is from Thompson et al. (1990). Optical ID is from Hewitt & Burbidge (1993).

J1549+0237.—A 5 GHz GOT image in 2000 (Mosoni et al. 2002) shows a jet extending to the south. The source underwent an outburst between 1996 and 1999 (Tingay et al. 2003).

J1613+3412.—Owing to the lack of data on shorter baselines the extended emission to the south, seen in the VLBA2cm1 and USNO images, is not seen in our image. The area subtended by the core is less than 0.07 mas^2.

J1617−7717.—An image from the complete GOT data set is given in VSOPsth. They identify the core as the weaker, more compact component to the east. The area subtended by the faint core is less than 0.9 mas^2.

J1626−2951.—See VSOPsth for the image with all the GOT data.

J1635+3808.—See VSOPPR for the image using the entire GOT data set. The area subtended by the faint core is less than 0.08 mas^2.

J1638+5720.—The core has been identified as the more northerly component in VSOPPR, where an image using the entire GOT data set can be found. The area subtended by the core is less than 0.4 mas^2.

J1642+3948.—(3C 345) A GOT image for this source can be found in VSOPPR.

J1642+6856.—An image with the full GOT data set is given in VSOPPR. In our image, the more northerly emission has been modeled by two unresolved components. As in VSOPPR, we have assumed the core is more northerly of these two components. The area subtended by this core component is less than 0.2 mas^2.

J1653+3945.—(Mrk 501) The GOT image for this source can be found in Edwards et al. (2000).

J1658+0515.—This source consists of two closely spaced components and is similar to that found in the VLBA2cm1. Since the extended emission is to the east (VLBApls and USNO), the core is probably the component to the west.

J1658+0741.—The emission near the source center contains two components. Presumably, the component to the southeast is the core. VLBApls, USNO, VLBA2cm1, and VLBA2cm2 images show a jet linking the core to the secondary component.

J1723−6500.—This is an extremely low-redshift GPS galaxy (Tingay et al. 1997). Since the core of GPS galaxies are usually weak, we have assumed that the core for this

source was undetected during the observation. Both components in our image are of similar strength.

J1733−1304.—(NRAO 530) There are no data on the short spacings, so the large-scale structure seen in other VLBI images is missing.

J1740+5221.—A GOT image can be found in VSOPPR.

J1800+7828.—A GOT image can be found in VSOPPR.

J1806+6949.—(3C 371) A GOT image can be found in VSOPPR.

J1824+5651.—A GOT image can be found in VSOPPR.

J1902+3159.—(3C 395) The core has been identified as the most westerly component by Lara et al. (1997).

J1924−2914.—The (u, v) plane coverage for this source is poor, so the much of the extended emission to the northeast is missing. For more detailed images of the extended emission see Shen et al. (1999), VLBApls, USNO, VLBA2cm1, and VLBA2cm2. The area subtended by the faint core is less than 0.1 mas^2.

J1939−1525.—The image found in VLBA2cm2 has an extra component to the east of the core.

J2005+7752.—The extended emission in the VLBApls, USNO, VLBA2cm1, and VLBA2cm2 images extends more directly toward the east.

J2022+6136.—This is a GPS source. Images of this source made from GOT data can be found in VSOPPR and Tschager et al. (2000). The core identification is from the latter reference.

J2101+0341.—The VLBA2cm2 image has a jet to the north-northeast, not seen in our image. The area subtended the unresolved core is less than 0.07 mas^2.

J2129−1538.—This is a GPS source (Stanghellini et al. 1997). The area subtended by the faint core is less than 0.05 mas^2.

J2136+0041.—This is a complex source. The structure is similar to that of the USNO and VLBA2cm1 images. Since most of the extended emission lies to the west we have assumed the core to be the easternmost component.

J2158−1501.—The area subtended by the faint core is less than 0.2 mas^2.

J2202+4216.—(BL Lac) A VSOP image made from GOT data can be found in Okayasu et al. (2000).

J2212+2355.—The data for this source are of poor quality, and the image has a relatively low resolution. The optical ID is from Condon et al. (1983).

J2229−0832.—Other VLBI images have an additional 1.2 Jy of integrated flux density, as well as extended emission to the north. ATCA monitoring (Tingay et al. 2003) indicates this source is highly variable at 4.8 GHz.

J2253+1608.—(3C 454.3) Although some of the large-scale emission is absent, our image is consistent with the bent-jet morphology seen in other VLBI images. Our model for this source includes VLBApls components 1,3 and 4.

J2320+0513.—Our image does not show the extended emission to the northwest seen in other VLBI images. The core region contains two components. The component to the southeast is probably the core.

J2329−4730.—The area subtended by this unresolved component is less than 0.1 mas^2.

J2331−1556.—The area subtended by the core is less than 0.2 mas^2.

J2348−1631.—The data quality for this source is poor but confirms the overall size and shape of the source found in the VLBApls, USNO, and VLBA2cm1 images. The area subtended by the core is less than 0.3 mas^2.

4. DISCUSSION

Of the 98 sources for which we were able to determine a source frame core brightness temperature, 53 had brightness temperatures in excess of the canonical inverse Compton limit of 10^{12} K. This is the theoretical upper limit on the brightness temperature for sources radiating incoherent synchrotron radiation (Kellermann & Pauliny-Toth 1969). Above this limit inverse Compton scattering leads to rapid cooling of the electron-photon plasma. Hence, explaining the high brightness temperatures requires other mechanisms, such as relativistic Doppler beaming. The maximum source frame brightness temperature we observed was 1.2×10^{13} K (for the source J0539−2839). This is below the highest core brightness temperature detected to date of 5.8×10^{13} K (for the BL Lac object AO 0235+164, Frey et al. 2000) but is well above the inverse Compton limit. The median source frame core brightness temperature of $\approx 10^{12}$ K is in good agreement with the preliminary results found by Lovell et al. (2000).

A statistical analysis of a somewhat larger sample of the VSOP Survey data is given by Horiuchi et al. (2004), who also model the angular size and brightness temperature distributions. This larger sample includes those sources which were found to be too resolved to be included in the VSOP source list. The brightness temperature and angular size distribution found at 15 GHz (Y. Y. Kovalev et al. 2004, in preparation) is also similar to those reported in this paper.

Because of the variability of many of the sources in the Survey sample, detailed spectral indices of the core components are difficult to determine. However, many of the sources were observed with the VLBA at 15 GHz as part of the VLBA2cm2 survey, and the spectral properties of the cores will be reported elsewhere (L. I. Gurvits et al. 2004, in preparation).

In conclusion, we find that about half of the AGN sample of sources reported upon in this paper have significant radio emission in the core component, with $T_b \approx 10^{12}$ K at 5 GHz in the source frame. Since the maximum brightness temperature one is able to determine using only ground-based arrays is of the order of 10^{12} K, our results confirm the necessity of using space VLBI to explore the extremely high brightness temperature regime. In addition, our Survey results clearly show that by using space VLBI with higher sensitivity, and somewhat higher resolution, the radio cores of many AGNs can be successfully imaged.

We gratefully acknowledge the VSOP Project, which is led by the Institute of Space and Astronautical Science of the Japan Aerospace Exploration Agency, in cooperation with many organizations and radio telescopes around the world. W. K. S. and A. R. T. wish to acknowledge support from the Canadian Space Agency. J. E. J. L. and G. A. M. acknowledge support from the Japan Society for the Promotion of Science. J. E. J. L. is also thankful for support from the Australian Commonwealth Scientific & Industrial Research Organization. R. D. is supported by a grant from the Japan Society for the Promotion of Science. S. H. acknowledges support through an NRC/NASA-JPL Research Associateship. S. F. acknowledges the Bolyai Scholarship received from the Hungarian Academy of Sciences. This research has made use of data from the University of Michigan Radio Astronomy Observatory, which is supported by funds from the University of Michigan, the United States Naval Observatory (USNO) Radio Reference

Frame Image Database (RRFID), and the NASA/IPAC Extragalactic Database (NED), which is operated by the Jet Propulsion Laboratory, California Institute of Technology, under contract with the National Aeronautics and Space Administration. The NRAO is a facility of the National Science Foundation, operated under cooperative agreement by Associated Universities, Inc. The Australia Telescope Compact Array is part of the Australia Telescope, which is funded by the Commonwealth of Australia for operation as a National Facility managed by CSIRO.

REFERENCES

Asada, K., Kameno, S., Inoue, M., Shen, Z.-Q., Horiuchi, S., & Gabuzda, D. C. 2000, in Proc. VSOP Symp., Astrophysical Phenomena Revealed by Space VLBI, ed. H. Hirabayashi, P. G. Edwards, & D. W. Murphy (Sagamihara: Institute of Space and Astronautical Science), 51
Condon, J. J., Condon, M. A., Broderick, J. J., & Davis, M. M. 1983, AJ, 88, 20
Drinkwater, M. J., et al. 1997, MNRAS, 284, 85
Edwards, P. G., Giovannini, G., Cotton, W. D., Feretti, L., Fujisawa, K., Hirabayashi, H., Lara, L., & Venturi, T. 2000, PASJ, 52, 1015
Edwards, P. G., Hirabayashi, H., Fomalont, E. B., Gurvits, L. I., Horiuchi, S., Lovell, J. E. J., Moellenbrock, G. A., & Scott, W. K. 2002, in ASP Conf. Ser. 289, Eighth IAU Asian-Pacific Meeting, Vol. II, ed. S. Ikeuchi, J. Hearnshaw, & T. Hanawa (San Francisco: ASP), 375
Fey, A. L., & Charlot, P. 1997, ApJS, 111, 95
———. 2000, ApJS, 128, 17
Fey, A. L., Clegg, A. W., & Fomalont, E. B. 1996, ApJS, 105, 299
Fomalont, E. B., Frey, S., Paragi, Z., Gurvits, L. I., Scott, W. K., Taylor, A. R., Edwards, P. G., & Hirabayashi, H. 2000a, ApJS, 131, 95
Fomalont, E., et al. 2000b, in Proc. VSOP Symp., Astrophysical Phenomena Revealed by Space VLBI, ed. H. Hirabayashi, P. G. Edwards, & D. W. Murphy (Sagamihara: Institute of Space and Astronautical Science), 167
Frey, S., Gurvits, L. I., Kellermann, K. I., Schilizzi, R. T., & Pauliny-Toth, I. I. K. 1997, A&A, 325, 511
Frey, S., et al. 2000, PASJ, 52, 975
Gabuzda, D. C., & Gómez, J. L. 2001, MNRAS, 320, L49
Gabuzda, D. C., Pushkarev, A. B., & Cawthorne, T. V. 1999, MNRAS, 307, 725
Gregory, P. C., Scott, W. K., Douglas, K., & Condon, J. J. 1996, ApJS, 103, 427
Greisen, E. W. 1988, in Acquisition, Processing and Archiving of Astronomical Images, ed. G. Longo & G. Sedmak (Napoli: Osservatorio Astronomico di Capodimonte), 125
Griffith, M. R., & Wright, A. E. 1993, AJ, 105, 1666
Hewitt, A., & Burbidge, G. 1987, ApJS, 63, 1
———. 1993, ApJS, 87, 451
Hirabayashi, H., et al. 1998, Science, 281, 1825
———. 2000a, PASJ, 52, 955
———. 2000b, PASJ, 52, 997 (Paper I)
Horiuchi, S., et al. 2004, ApJ, 616, in press (Paper IV)
Jackson, C. A., Wall, J. V., Shaver, P. A., Kellermann, K. I., Hook, I. M., & Hawkins, M. R. S. 2002, A&A, 386, 97
Junor, W., Biretta, J. A., Owen, F. N., & Begelman, M. C. 2000, in Proc. VSOP Symp. Astrophysical Phenomena Revealed by Space VLBI, ed. H. Hirabayashi, P. G. Edwards, & D. W. Murphy (Sagamihara: Institute of Space and Astronautical Science), 13
Kellermann, K. I., & Pauliny-Toth, I. I. K. 1969, ApJ, 155, L71
Kellermann, K. I., Vermeulen, R. C., Zensus, J. A., & Cohen, M. H. 1998, AJ, 115, 1295
Lara, L., Muxlow, T. W. B., Alberdi, A., Marcaide, J. M., Junor, W., & Saikia, D. J. 1997, A&A, 319, 405
Lawrence, C. R., Bennet, C. L., Hewitt, J. N., Langston, G. I., Klotz, S. E., Burke, B. F., & Turner, K. C. 1986, ApJS, 61, 105
Lawrence, C. R., Zucker, J. R., Readhead, C. S., Unwin, S. C., Pearson, T. J., & Xu, W. 1996, ApJS, 107, 541
Levy, G. S., et al. 1989, ApJ, 336, 1098
Linfield, R. P., et al. 1989, ApJ, 336, 1105
———. 1990, ApJ, 358, 350
Lister, M. L., Tingay, S. J., Murphy, D. W., Piner, B. G., Jones, D. L., & Preston, R. A. 2001, ApJ, 554, 948
Lobanov, A. P., & Zensus, J. A. 2001, Science, 294, 128
Lovell, J. E. J. 2000, in Proc. VSOP Symp., Astrophysical Phenomena Revealed by Space VLBI, ed. H. Hirabayashi, P. G. Edwards, & D. W. Murphy (Sagamihara: Institute of Space and Astronautical Science), 301
Lovell, J. E. J., et al. 2000, in Proc. VSOP Symp., Astrophysical Phenomena Revealed by Space VLBI, ed. H. Hirabayashi, P. G. Edwards, & D. W. Murphy (Sagamihara: Institute of Space and Astronautical Science), 183
———. 2004, ApJS, 155, in press (Paper II)
Moellenbrock, G. A., et al. 2000, in Proc. VSOP Symp., Astrophysical Phenomena Revealed by Space VLBI, ed. H. Hirabayashi, P. G. Edwards, & D. W. Murphy (Sagamihara: Institute of Space and Astronautical Science), 177
Mosoni, L., Frey, S., Paragi, Z., Fejes, I., Edwards, P. G., Fomalont, E. B., Gurvits, L. I., & Scott, W. K. 2002, in Proc. Sixth European VLBI Network Symp., ed. E. Ros, R. W. Porcas, A. P. Lobanov, & J. A. Zensus (Bonn: Max-Planck-Institute für Radioastronomie), 97
Okayasu, R., et al. 2000, Adv. Space Res., 26, 681
Pearson, T. J., & Readhead, C. S. 1988, ApJ, 328, 114
Piner, B. G., Edwards, P. G., Wehrle, A. E., Hirabayashi, H., Lovell, J. E. J., & Unwin, S. C. 2000, ApJ, 537, 91
Shen, Z.-Q., Edwards, P. G., Lovell, J. E. J., Fujisawa, K., Kameno, S., & Makoto, I. 1999, PASJ, 51, 513
Shepherd, M. C. 1997, in ASP Conf. Ser. 125, Astronomical Data Analysis Software and Systems VI, ed. J. A. Zensus, G. B. Taylor, & J. M. Wrobel (San Francisco: ASP), 77
Slysh, V. I., et al. 2001, Astron. Lett., 27, 277
Stanghellini, C., O'Dea, C. P., Baum, S. A., Fanti, R., & Fanti, C. 1997, A&A, 325, 943
Stickel, M., & Kühr, H. 1996, A&A, 115, 11
Thompson, D. J., Djorgovski, S., & De Carvalho, R. 1990, PASP, 102, 1235
Tingay, S. J., Jauncey, D. L., King, E. A., Tzioumis, A. K., Lovell, J. E. J., & Edwards, P. G. 2003, PASJ, 55, 351
Tingay, S. J., et al. 1997, AJ, 113, 2025
———. 2001, ApJ, 549, L55
———. 2002, ApJS, 141, 311
Tschager, W., Schilizzi, R. T., Röttgering, H. J. A., Snellen, I. A. G., & Miley, G. K. 2000, A&A, 360, 887
Tzioumis, A. K., et al. 1989, AJ, 98, 36
Vermeulen, R. C., Readhead, C. S., & Backer, D. C. 1994, ApJ, 430, L41
Véron-Cetty, M.-P., & Véron, P. 2001, A&A, 374, 92
Zensus, J. A., Ros, E., Kellermann, K. I., Cohen, M. H., Vermeulen, R. C., & Kadler, M. 2002, AJ, 124, 662